

## BLAST: the far-infrared/radio correlation in distant galaxies

R. J. Ivison,<sup>1,2\*</sup> David M. Alexander,<sup>3</sup> Andy D. Biggs,<sup>4</sup> W. N. Brandt,<sup>5</sup>  
Edward L. Chapin,<sup>6</sup> Kristen E. K. Coppin,<sup>3</sup> Mark J. Devlin,<sup>7</sup> Mark Dickinson,<sup>8</sup>  
James Dunlop,<sup>2</sup> Simon Dye,<sup>9</sup> Stephen A. Eales,<sup>9</sup> David T. Frayer,<sup>10</sup> Mark Halpern,<sup>6</sup>  
David H. Hughes,<sup>11</sup> Edo Ibar,<sup>1</sup> A. Kovács,<sup>12</sup> Gaelen Marsden,<sup>6</sup> L. Moncelsi,<sup>9</sup>  
Calvin B. Netterfield,<sup>13,14</sup> Enzo Pascale,<sup>9</sup> Guillaume Patanchon,<sup>15</sup> D. A. Rafferty,<sup>5</sup>  
Marie Rex,<sup>7</sup> Eva Schinnerer,<sup>16</sup> Douglas Scott,<sup>6</sup> C. Semisch,<sup>7</sup> Ian Smail,<sup>3</sup>  
A. M. Swinbank,<sup>3</sup> Matthew D. P. Truch,<sup>7</sup> Gregory S. Tucker,<sup>17</sup> Marco P. Viero,<sup>14</sup>  
Fabian Walter,<sup>16</sup> Axel Weiß,<sup>12</sup> Donald V. Wiebe,<sup>6,14</sup> and Y. Q. Xue<sup>5</sup>

<sup>1</sup>UK Astronomy Technology Centre, Royal Observatory, Blackford Hill, Edinburgh EH9 3HJ

<sup>2</sup>Institute for Astronomy, University of Edinburgh, Blackford Hill, Edinburgh EH9 3HJ

<sup>3</sup>Institute for Computational Cosmology, Durham University, South Road, Durham DH1 3LE

<sup>4</sup>European Southern Observatory, Karl-Schwarzschild-Str. 2, D-85748, Germany

<sup>5</sup>Department of Astronomy and Astrophysics, The Pennsylvania State University, University Park, PA 16802, USA

<sup>6</sup>Department of Physics & Astronomy, University of British Columbia, 6224 Agricultural Road, Vancouver, BC V6T 1Z1, Canada

<sup>7</sup>Department of Physics & Astronomy, University of Pennsylvania, 209 South 33rd Street, Philadelphia, PA, 19104, USA

<sup>8</sup>NOAO, 950 N. Cherry Avenue, Tucson, AZ 85719, USA

<sup>9</sup>School of Physics and Astronomy, Cardiff University, Queens Buildings, The Parade, Cardiff CF24 3AA

<sup>10</sup>Spitzer Science Center, California Institute of Technology, Pasadena, CA 91125, USA

<sup>11</sup>Instituto Nacional de Astrofísica Óptica y Electrónica, Aptdo. Postal 51 y 72000 Puebla, Mexico

<sup>12</sup>Max-Planck Institute für Radioastronomie, D-53121 Bonn, Germany

<sup>13</sup>Department of Astronomy & Astrophysics, University of Toronto, 50 St. George Street Toronto, ON M5S 3H4, Canada

<sup>14</sup>Department of Physics, University of Toronto, 60 St. George Street, Toronto, ON M5S 1A7, Canada

<sup>15</sup>Laboratoire APC, 10, rue Alice Domon et Léonie Duquet, 75205 Paris, France

<sup>16</sup>Max-Planck-Institut für Astronomie, Königstuhl 17, D-69117 Heidelberg, Germany

<sup>17</sup>Department of Physics, Brown University, 182 Hope Street, Providence, RI 02912, USA

Accepted 2009 October 22. Received 2009 October 19; in original form 2009 July 14

### ABSTRACT

We investigate the correlation between far-infrared (FIR) and radio luminosities in distant galaxies, a lynchpin of modern astronomy. We use data from the Balloon-borne Large Aperture Submillimetre Telescope (BLAST), *Spitzer*, the Large Apex BOlometer CamerA (LABOCA), the Very Large Array and the Giant Metre-wave Radio Telescope (GMRT) in the Extended *Chandra* Deep Field South (ECDFS). For a catalogue of BLAST 250- $\mu\text{m}$ -selected galaxies, we remeasure the 70–870- $\mu\text{m}$  flux densities at the positions of their most likely 24- $\mu\text{m}$  counterparts, which have a median [interquartile] redshift of 0.74 [0.25, 1.57]. From these, we determine the monochromatic flux density ratio,  $q_{250}(=\log_{10}[S_{250\mu\text{m}}/S_{1400\text{MHz}}])$ , and the bolometric equivalent,  $q_{\text{IR}}$ . At  $z \approx 0.6$ , where our 250- $\mu\text{m}$  filter probes rest-frame 160- $\mu\text{m}$  emission, we find no evolution relative to  $q_{160}$  for local galaxies. We also stack the FIR and submm images at the positions of 24- $\mu\text{m}$ - and radio-selected galaxies. The difference between  $q_{\text{IR}}$  seen for 250- $\mu\text{m}$ - and radio-selected galaxies suggests that star formation provides most of the IR luminosity in  $\lesssim 100\text{-}\mu\text{Jy}$  radio galaxies, but rather less for those in the mJy regime. For the 24- $\mu\text{m}$  sample, the radio spectral index is constant across  $0 < z < 3$ , but  $q_{\text{IR}}$  exhibits tentative evidence of a steady decline such that  $q_{\text{IR}} \propto (1+z)^{-0.15 \pm 0.03}$  – significant evolution, spanning the epoch of galaxy formation, with major implications for techniques that rely on the FIR/radio correlation. We compare with model predictions and speculate that we may be seeing the increase in radio activity that gives rise to the radio background.

**Key words:** galaxies: evolution – infrared: galaxies – radio continuum: galaxies.

\*E-mail: rji@roe.ac.uk

## 1 INTRODUCTION

The correlation between far-infrared (FIR) and radio luminosities (e.g. van der Kruit 1971; Dickey & Salpeter 1984; de Jong et al. 1985; Helou, Soifer & Rowan-Robinson 1985) is believed to be due to a common link with massive, dust-enshrouded stars. During their brief lives these stars warm the dusty molecular clouds in which they were born, expel dust in their winds, then create radio-luminous supernova remnants (which are believed to accelerate cosmic ray electrons), perhaps generating more dust during this finale (e.g. Dunne et al. 2009b).

The empirical FIR/radio correlation is regularly exploited in a variety of ways – to calibrate the relationship between radio luminosity and star-formation rate (SFR; Condon 1992; Bell 2003), for example, or to estimate the distance to luminous starbursts (e.g. Carilli & Yun 1999) or their dust temperatures ( $T_d$  – e.g. Chapman et al. 2005) or to define samples of radio-excess active galactic nuclei (AGN; e.g. Donley et al. 2005). The correlation has thus become a cornerstone of modern astronomy. It is clearly important to know whether the correlation breaks down at extreme luminosities, or varies with redshift, perhaps due to variations in magnetic field strength (e.g. Bernet et al. 2008), IR photon density, initial mass function (IMF), dust composition or cosmic ray flux (e.g. Rengarajan 2005).

Recent efforts have concentrated on determining the relationship between radio and 24- $\mu\text{m}$  flux densities,  $q_{24} = \log_{10}(S_{24\mu\text{m}}/S_{1400\text{MHz}})$ , taking advantage of *Spitzer*'s sensitivity to hot dust emission from very distant star-forming galaxies (e.g. Appleton et al. 2004; Ibar et al. 2008). A galaxy's 24- $\mu\text{m}$  luminosity is not a particularly reliable tracer of its FIR luminosity, however, being prone to uncertain contamination by AGN continuum emission and by spectral features due to silicates and polycyclic aromatic hydrocarbons (Pope et al. 2006; Desai et al. 2007).

Appleton et al. noted that 'ideally, it would be better to measure a bolometric  $q$ , but insufficient data are available at longer wavelengths to do this reliably'. Here, we exploit new data from Balloon-borne Large Aperture Submillimetre Telescope (BLAST; Devlin et al. 2009) and the Large Apex BOlometer Camera (LABOCA) Extended *Chandra* Deep Field South (ECDFS) Submm Survey (LESS; Weiss et al. 2009) to explore the correlation between *bolometric* IR luminosity and  $K$ -corrected radio luminosity. We do this separately for FIR-, 24- $\mu\text{m}$ - and radio-selected galaxies. The latter categories are explored in Section 4.4, stacking at the positions of 24- $\mu\text{m}$  and radio emitters.

Before we describe our analysis, the question of how best to explore the FIR/radio correlation for FIR-selected galaxies merits discussion. A thorough treatment of the IR and radio properties of FIR-selected galaxies must be able to deal with the potentially FIR-loud and radio-weak fractions of the sample. If the available FIR data were well matched in resolution to typical optical/IR or radio imaging then comparing FIR and radio properties would be trivial. As things stand, however, the BLAST 250- $\mu\text{m}$  beam covers  $\sim 500\times$  more area than a typical Very Large Array (VLA) synthesized beam and matching FIR and radio sources is non-trivial (Section 3.1).

We must consider how to deal with cases where counterparts to our FIR emitters cannot be found. This leaves us with no way to determine their positions unambiguously or even their FIR flux densities since they are often blended or their radio flux densities (or appropriate limits) or their redshifts. We can not begin the analysis by pinpointing the FIR emitters in the radio waveband since this introduces a strong bias in favour of the most luminous radio emitters. Marsden et al. (2009) showed that the 24- $\mu\text{m}$  galaxy pop-

ulation detected by *Spitzer* (Magnelli et al. 2009) can account for all of the FIR background, as measured by the *Cosmic Background Explorer* (Puget et al. 1996; Fixsen et al. 1998). We have already noted that the correlation between 24- $\mu\text{m}$  and FIR luminosities is poor, but every FIR source should have a 24- $\mu\text{m}$  counterpart and our approach to pinning down the positions and radio properties of the parent sample is to adopt the 24- $\mu\text{m}$  identifications proposed by Dye et al. (2009) or, where Dye et al. opts for a radio identification, our own 24- $\mu\text{m}$  identifications. Armed with these positions, we determine the radio properties and redshifts of the appropriate counterparts, including appropriate limits for any that lack radio emission.

Our paper is laid out as follows. In Section 2, we introduce a 250- $\mu\text{m}$ -selected sample of galaxies from BLAST and the *Spitzer*, LABOCA, VLA and Giant Metre-wave Radio Telescope (GMRT) data used to determine their IR and radio spectral energy distributions (SEDs). In Section 3.1, we cross-match our FIR sample with radio emitters, demonstrating how difficult this will be for deep surveys with *Herschel*. We cross-match with the most likely 24- $\mu\text{m}$  counterparts (Section 3.2), enabling us to explore the FIR/radio correlation for our 250- $\mu\text{m}$ -selected galaxies in Section 4, unbiased by radio selection. We also investigate the correlation for 24- $\mu\text{m}$ - and radio-selected samples (Sections 4.4 and 4.5), via the stacking technique (e.g. Ivison et al. 2007a; Dunne et al. 2009a; Marsden et al. 2009), looking at the effect of  $K$ -corrections using several SED templates. We state our conclusions in Section 5.

Throughout this paper, we assume a Universe with  $\Omega_m = 0.27$ ,  $\Omega_\Lambda = 0.73$  and  $H_0 = 71 \text{ km s}^{-1} \text{ Mpc}^{-1}$  (Spergel et al. 2007).

## 2 OBSERVATIONS

Our primary data set, known as 'BLAST GOODS South – Deep' (where GOODS is the Great Observatories Origins Deep Survey; Dickinson, Giavalisco & The Goods Team 2003), was taken during BLAST's Antarctic flight in 2006 (Devlin et al. 2009) and comprises maps<sup>1</sup> covering the ECDFS at 250, 350 and 500  $\mu\text{m}$ . We combine them with panchromatic data, including the deepest available 70–160- $\mu\text{m}$  imaging from *Spitzer* – from the FIR Deep Extragalactic Legacy survey (FIDEL), with 870- $\mu\text{m}$  LABOCA imaging from the 12-m Atacama Pathfinder EXperiment (APEX) telescope (Weiss et al. 2009), with high-resolution 1400-MHz imaging from the VLA (Miller et al. 2008; Biggs et al., in preparation) and with new 610-MHz imaging from the GMRT. This latter data set allows us to  $K$ -correct the 1400-MHz radio luminosity accurately out to  $z \sim 1.3$ , and beyond if the spectra are intrinsic power laws. Previous work assumes radio emitters share a common spectral index,  $\alpha \approx -0.8$  (where  $S \propto \nu^\alpha$ ) – a poor approximation, as shown by Ibar et al. (2009). Together, these data are capable – prior to operations with *Herschel* – of determining the bolometric IR luminosities of distant galaxies.

In order to take full advantage of the best available multiwavelength coverage, we limit the areal coverage of this study to that of the deep VLA imaging described in Section 2.4, a region of radius 17.2 arcmin centred on  $\alpha_{J2000} = 03^{\text{h}}32^{\text{m}}28^{\text{s}}.3$ ,  $\delta_{J2000} = -27^\circ48'30''$  (see Fig. 1). This area coincides with the deepest of the BLAST surveys.

<sup>1</sup> Available at <http://blastexperiment.info>

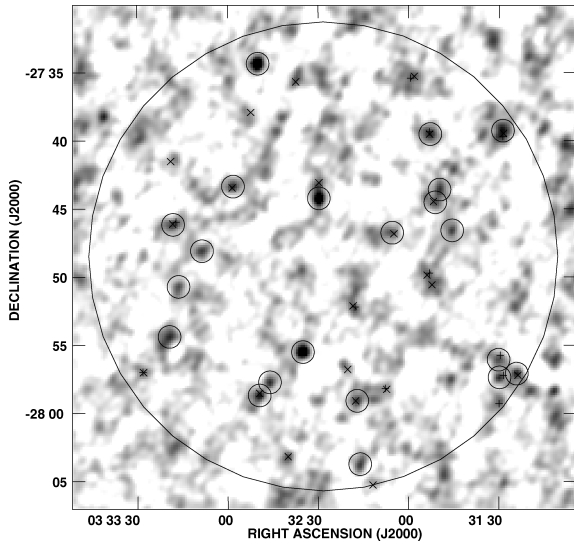


**Figure 1.** BLAST 250- $\mu\text{m}$  image of the central region of ECDFS, with  $> 3\sigma$  sources circled.  $\sigma$  includes instrumental and confusion noise combined in quadrature, where  $\sigma_{\text{confusion}}/\sigma_{\text{instrumental}} \sim 2$  (Marsden et al. 2009). For the deepest imaging planned for *Herschel*, this ratio will be  $\approx 25$ . Similarly significant sources at 350 and 500  $\mu\text{m}$  are labelled with  $\times$  and  $+$  symbols, respectively. The region covered by the deepest VLA imaging, with relatively low levels of bandwidth smearing, is within the 17.2-arcmin-radius circle.

## 2.1 BLAST 250-, 350- and 500- $\mu\text{m}$ measurements

The 1.8-m BLAST is a forerunner of the Spectral and Photometric Imaging Receiver (SPIRE; Griffin et al. 2009) on the 3.5-m *Herschel Space Observatory*. Data here are from the successful 2006 flight, lasting 270 h, of which 90 h was spent surveying a field centred on the ECDFS.

In the part of this survey used here, the mean instrumental [confusion] noise levels are 11 [21], 9 [17] and 6 [15]  $\text{mJy beam}^{-1}$  at 250, 350 and 500  $\mu\text{m}$ , respectively, where the beams had full width at half-maximum (FWHM) of 36, 42 and 60 arcsec (Devlin et al. 2009; Marsden et al. 2009) and the noise values were determined in beam-smoothed maps.

As our parent catalogue we adopt the sample of 250- $\mu\text{m}$  BLAST sources described by Devlin et al. (2009), cutting at a signal-to-noise ratio (SNR) of three, where the uncertainty in flux comprised the quadrature sum of the instrumental noise (used to define SNR in the Devlin et al. catalogue) and the confusion noise. The reliability of our sample is thus similar to those of the first submm galaxy (SMG) catalogues (e.g. Smail, Ivison & Blain 1997; Barger et al. 1998; Hughes et al. 1998). Thus defined, our parent catalogue comprises 22 sources, listed in Table 1 and marked in Fig. 1.

For the FIR measurements described in the sections that follow, the BLAST image in each of the three filters has been convolved with the appropriate noise-weighted point spread function (PSF; Truch et al. 2009). This is equivalent to calculating the maximum-likelihood point-source flux density by which the PSF would have been scaled to fit an isolated point source centred in each pixel. Flux densities in each band are taken from these convolved maps at the appropriate positions.

Since the differential 250- $\mu\text{m}$  source counts fall rapidly with flux  $dN/dS \propto S^{-3.5}$  – see Patanchon et al. (2009), the effects of Eddington bias and source confusion have conspired to boost the fluxes in our parent catalogue. To determine the degree of boosting, we simulate these effects by injecting a source population consistent

with the BLAST counts (Patanchon et al. 2009) into a Gaussian noise field resembling the instrumental fluctuations in the BLAST GOODS South – Deep field and then measuring the flux densities of those sources at the input positions (see appendix B of Eales et al. 2009). These simulations allow us to apply appropriate first-order corrections and to estimate the uncertainties associated with those corrections (see later in Section 4.2). The corrections are statistical in nature and can be tailored to individual sources only in the sense that a source with a given SNR is likely to have been boosted by factor,  $B(\text{SNR})$ , where  $B$  ranges from  $\sim 1.1$  to 1.6 for the range of SNRs present in our sample. A full treatment of flux boosting in the BLAST data – including the influence of clustering and multiband source selection – will be explored in future work.

## 2.2 *Spitzer* 70- and 160- $\mu\text{m}$ measurements

All of the raw FIDEL (P.I.: Dickinson), GO (P.I.: Frayer) and GTO (P.I.: Rieke) *Spitzer* data covering ECDFS were reduced and combined using the techniques developed by Frayer et al. (2006). We adopted the updated calibration factors, including corrections for colour and for the point-source-response function given by Frayer et al. (2009).

The *Spitzer* flux density measurements are made at the positions discussed later and the quoted uncertainties represent the rms noise at those positions, combined with an additional 10 (15) per cent uncertainty at 70  $\mu\text{m}$  (160  $\mu\text{m}$ ) due to possible systematics affecting the calibration factors.

## 2.3 LABOCA 870- $\mu\text{m}$ measurements

LESS covers around  $900 \text{ arcmin}^2$  of ECDFS at a wavelength of 870  $\mu\text{m}$ , with a beamwidth of 19.2 arcsec FWHM (Coppin et al. 2009; Greve et al. 2009; Weiss et al. 2009), to an average depth of  $\sigma = 1.2 \text{ mJy beam}^{-1}$  as measured in a beam-smoothed map across the region in which our 250- $\mu\text{m}$  sample was selected. The 870- $\mu\text{m}$  flux densities, at the positions discussed later, are measured in the same manner discussed in Sections 2.1 and 2.2.

## 2.4 VLA 1400-MHz imaging

Deep, high-resolution 1400-MHz imaging of the ECDFS was described by Miller et al. (2008), and we use their image to identify radio counterparts for our parent 250- $\mu\text{m}$ -selected source catalogue (see Section 3).

We use the techniques described by Ibar et al. (2009) to generate a new, deeper 1400-MHz catalogue and to correct for effects such as flux boosting at low SNRs. This catalogue was cut at  $> 4\sigma$ , where  $\sigma$  was determined from the local background.

In cases, where the emission is found to be heavily resolved, e.g. for the large spiral associated with BLAST J033235–275530, we measure the total radio flux density using TVSTAT within *aips*.

## 2.5 GMRT 610-MHz imaging

To test the feasibility of deep radio observations in ECDFS, a small amount of new 610-MHz data were obtained using the GMRT<sup>2</sup> in 2008 November. During seven 9-h sessions, we obtained data

<sup>2</sup>We thank the staff of the GMRT who made these observations possible. GMRT is run by the National Centre for Radio Astrophysics of the Tata Institute of Fundamental Research.

**Table 1.** Parent 250- $\mu$ m catalogue from BLAST (Devlin et al. 2009), 24- $\mu$ m identifications, radio and X-ray properties, and redshifts.

| BLAST name     | $\alpha_{250\mu\text{m}}$<br>J2000 | $\delta_{250\mu\text{m}}$<br>J2000 | $S_{250\mu\text{m}}^{\dagger}$<br>mJy | $\alpha_{24\mu\text{m}}$<br>J2000 | $\delta_{24\mu\text{m}}$<br>J2000 | $S_{24\mu\text{m}}$<br>mJy | $S_{1400\text{MHz}}$<br>$\mu$ Jy | $S_{610\text{Hz}}$<br>$\mu$ Jy | $\alpha_{610}^{1400}$ | X-ray? <sup>‡</sup> | Spec<br>z | Phot<br>z |
|----------------|------------------------------------|------------------------------------|---------------------------------------|-----------------------------------|-----------------------------------|----------------------------|----------------------------------|--------------------------------|-----------------------|---------------------|-----------|-----------|
| J033235–275530 | 03:32:35.09                        | –27:55:31.0                        | 176.8 $\pm$ 10.9                      | 03:32:35.07                       | –27:55:32.6                       | 4.7                        | 680 $\pm$ 34*                    | 565 $\pm$ 99                   | +0.22                 | Y                   | 0.038     | 0.051     |
| J033229–274414 | 03:32:29.74                        | –27:44:14.4                        | 156.7 $\pm$ 10.9                      | 03:32:29.87                       | –27:44:24.2                       | 11.1                       | 1,558 $\pm$ 55*                  | 1,670 $\pm$ 84                 | –0.08                 | Y                   | 0.077     | 0.077     |
| J033250–273421 | 03:32:50.01                        | –27:34:21.3                        | 159.3 $\pm$ 11.1                      | 03:32:50.41                       | –27:34:20.3                       | 2.9                        | 470 $\pm$ 20*                    | 706 $\pm$ 56                   | –0.49                 | N                   | 0.251     | 0.251     |
| J033128–273916 | 03:31:28.71                        | –27:39:16.1                        | 105.3 $\pm$ 11.1                      | 03:31:28.82                       | –27:39:16.7                       | 0.46                       | 34.8 $\pm$ 7.5                   | 3 $\sigma$ < 150               | –0.80                 | N                   | —         | —         |
| J033249–275842 | 03:32:49.47                        | –27:58:42.0                        | 101.2 $\pm$ 11.0                      | 03:32:49.34                       | –27:58:44.7                       | 0.32                       | 216 $\pm$ 16                     | 296 $\pm$ 49                   | –0.38                 | N                   | —         | 2.215     |
| J033124–275705 | 03:31:24.05                        | –27:57:05.5                        | 96.3 $\pm$ 11.1                       | 03:31:23.48                       | –27:56:58.5                       | 1.3                        | 165 $\pm$ 16                     | 183 $\pm$ 52                   | –0.12                 | N                   | —         | 2.732     |
| J033152–273931 | 03:31:52.82                        | –27:39:31.5                        | 93.4 $\pm$ 11.0                       | 03:31:52.07                       | –27:39:26.6                       | 0.20                       | 965 $\pm$ 16                     | 765 $\pm$ 52                   | +0.28                 | Y                   | —         | 2.296     |
| J033258–274322 | 03:32:58.24                        | –27:43:22.3                        | 92.6 $\pm$ 11.1                       | 03:32:59.20                       | –27:43:25.1                       | 0.53                       | 148 $\pm$ 17                     | 205 $\pm$ 43                   | –0.39                 | N                   | —         | 1.160     |
| J033129–275722 | 03:31:29.79                        | –27:57:22.6                        | 91.6 $\pm$ 11.0                       | 03:31:29.92                       | –27:57:22.4                       | 0.27                       | 144 $\pm$ 16                     | 169 $\pm$ 51                   | –0.19                 | N                   | —         | 1.571     |
| J033319–275423 | 03:33:19.37                        | –27:54:23.2                        | 90.7 $\pm$ 10.9                       | 03:33:18.89                       | –27:54:33.8                       | 0.37                       | 60.2 $\pm$ 15.0                  | 3 $\sigma$ < 150               | –0.80                 | N                   | —         | 0.488     |
| J033246–275744 | 03:32:46.05                        | –27:57:44.0                        | 90.0 $\pm$ 10.9                       | 03:32:45.88                       | –27:57:44.8                       | 2.7                        | 337 $\pm$ 17*                    | 364 $\pm$ 89                   | –0.09                 | Y                   | 0.103     | 0.105     |
| J033149–274335 | 03:31:49.71                        | –27:43:35.9                        | 86.6 $\pm$ 11.0                       | 03:31:49.69                       | –27:43:26.4                       | 0.95                       | 192 $\pm$ 16                     | 271 $\pm$ 97                   | –0.41                 | N                   | 0.618     | 0.603     |
| J033217–275905 | 03:32:17.07                        | –27:59:05.8                        | 85.3 $\pm$ 11.0                       | 03:32:16.99                       | –27:59:16.0                       | 0.37                       | 178 $\pm$ 17                     | 395 $\pm$ 45                   | –0.96                 | N                   | 0.126     | 0.220     |
| J033318–274610 | 03:33:18.13                        | –27:46:10.3                        | 82.6 $\pm$ 10.9                       | 03:33:17.78                       | –27:46:05.9                       | 0.43                       | 100 $\pm$ 14                     | 194 $\pm$ 48                   | –0.80                 | N                   | —         | 2.059     |
| J033216–280345 | 03:32:16.08                        | –28:03:45.0                        | 82.1 $\pm$ 11.0                       | 03:32:15.90                       | –28:03:47.1                       | 0.77                       | 192 $\pm$ 20                     | 268 $\pm$ 49                   | –0.40                 | N                   | —         | 0.452     |
| J033145–274635 | 03:31:45.54                        | –27:46:35.5                        | 80.2 $\pm$ 10.9                       | 03:31:45.36                       | –27:46:40.2                       | 0.29                       | 42.2 $\pm$ 7.3                   | 171 $\pm$ 53                   | –1.68                 | N                   | —         | —         |
| J033308–274805 | 03:33:08.56                        | –27:48:05.9                        | 79.7 $\pm$ 10.8                       | 03:33:09.72                       | –27:48:01.3                       | 0.20                       | 433 $\pm$ 19                     | 496 $\pm$ 45                   | –0.16                 | N                   | 0.180     | 0.190     |
| J033151–274431 | 03:31:51.15                        | –27:44:31.8                        | 74.0 $\pm$ 10.9                       | 03:31:51.09                       | –27:44:37.1                       | 0.52                       | 96.3 $\pm$ 13                    | 3 $\sigma$ < 150               | –0.53                 | Y                   | —         | 1.911     |
| J033130–275604 | 03:31:30.07                        | –27:56:04.5                        | 74.0 $\pm$ 10.9                       | 03:31:30.05                       | –27:56:02.2                       | 0.90                       | 1,270 $\pm$ 64*                  | 1,330 $\pm$ 67                 | –0.06                 | Y                   | 0.677     | 0.727     |
| J033218–275216 | 03:32:18.03                        | –27:52:16.8                        | 73.6 $\pm$ 10.9                       | 03:32:18.25                       | –27:52:24.9                       | 0.21                       | 23.7 $\pm$ 7.2                   | 3 $\sigma$ < 150               | –0.80                 | N                   | 0.739     | 0.724     |
| J033240–280314 | 03:32:40.11                        | –28:03:14.7                        | 72.7 $\pm$ 11.0                       | 03:32:39.69                       | –28:03:10.5                       | 0.34                       | 168 $\pm$ 30*                    | 707 $\pm$ 180                  | –1.73                 | N                   | —         | 0.956     |
| J033145–274205 | 03:31:45.02                        | –27:42:05.2                        | 72.8 $\pm$ 11.0                       | 03:31:44.46                       | –27:42:12.0                       | 0.43                       | 122 $\pm$ 19                     | 181 $\pm$ 45                   | –0.47                 | N                   | —         | 1.056     |

Notes: – <sup>†</sup>Flux densities before deboosting (see Section 4.2); these uncertainties include only instrumental noise (Section 2.1) and should be added in quadrature with the confusion noise ( $\sigma_{\text{confusion}} = 21.4$  mJy – Marsden et al. 2009) to arrive at realistic SNRs. \*Total flux density, determined using TVSTAT. <sup>‡</sup>24- $\mu$ m position coincident – within 2 arcsec – of a *Chandra* source (Lehmer et al. 2005; Luo et al. 2008). No further matches are made if the search radius is doubled.

centred on the six positions chosen by Miller et al. (2008) for their VLA survey (Section 2.4), recording 128 channels every 16 s in the lower and upper sidebands (602 and 618 MHz, respectively) in each of two polarizations. The integration time in each field was  $\sim 3$  h, made up of 30-min scans sandwiched between 5-min scans of the nearby calibrator, 0240–231, with 10-min scans of 3C 48 and 3C 147 for flux and bandpass calibration.

Calibration followed standard recipes within *aips* (31DEC09). A bandpass table was generated after self-calibrating 3C 48 and 3C 147 in phase with a solution interval of 1 min. This was applied during subsequent loops of calibration and flagging (with UVFLG, TVFLG, SPFLG and FLGIT). The error-weighted flux densities of 0240–231 were found to be  $5.55 \pm 0.02$  and  $5.31 \pm 0.02$  Jy at 602 and 618 MHz, respectively; the rms scatter of the flux density measurements over the seven days was 0.12 and 0.10 Jy which suggests that the flux calibration should be accurate to better than 5 per cent.

The calibrated data were averaged down to yield 41 channels in each sideband and the data from the seven days were concatenated using DBCON. The resulting data sets were then self-calibrated in phase (SOLMODE=P!A), with a solution interval of 2 min, using CLEAN components from our own reduction of the VLA A-configuration data. This process yielded accurate phases; the astrometric reference frame was also tied to that of the 1400-MHz image as a result. Subsequent imaging entailed the creation of a mosaic of 37 facets – to cover most of the primary beam in each of the six pointings – each facet with  $512^2$  pixels ( $1.5^2$  arcsec $^2$  pixel $^{-1}$ ). A further 10–20 bright sources outside these central regions, identified in heavily tapered maps, were also imaged for each pointing. Subsequent self-calibration was carried out in phase alone, then in amplitude and phase (first with CPARM = 0, 1, 0 then with CPARM = 0), with a solution interval of 2 min, staggered by 1 min. The *uv* data were weighted using ROBUST = –0.5, UVRANGE = 0.9, 100 k $\lambda$ , GUARD = –1, UVTAPER = 30, 60 k $\lambda$  and UVBOX = 10.

After CLEAN components were subtracted from the *uv* data, more manual flagging was undertaken. Almost one-third of the baselines were rejected, in total. CLEAN components were re-introduced (UVSUB, FACTOR=–1), then the final six mosaics were convolved to a common beam size ( $6.5 \times 5.4$  arcsec $^2$ , with the major axis at position angle  $174^\circ$ ), then knitted together using FLATN. An appropriate correction was made for the shape of the primary beam, with data rejected at radii beyond the half-maximum level. The final image has a noise level of  $\sim 40$   $\mu$ Jy beam $^{-1}$  and covers the entire VLA image, with insignificant levels of bandwidth smearing. We exploit it here to determine the 610-MHz flux densities, and hence the spectral indices between 610 and 1400 MHz,  $\alpha_{610}^{1400}$ , of the radio identifications described in Section 3. These measurements are listed in Table 1. Our 610-MHz image is available on request.<sup>3</sup>

### 3 IDENTIFICATIONS

In order to avoid introducing a strong radio-related bias, and despite the problems caused by the high surface density of 24- $\mu$ m emitters (evident in Fig. 2), we use the 24- $\mu$ m counterpart identifications of Dye et al. (2009) for our parent sample. Where Dye et al. does not present an association, or where they favour a radio identification over a 24- $\mu$ m source, we adopt our own 24- $\mu$ m identifications based on the probabilistic approach outlined in the next section.

Before we discuss the 24- $\mu$ m identifications – and although we do not use them hereafter – we first describe the identification of radio

counterparts to the parent FIR catalogue. Radio imaging remains the ‘gold standard’ for pinpointing submm and FIR galaxies because of the tight flux correlation and the low surface density of radio emitters relative to optical/IR sources, and relative to the large submm beam sizes. It is important, therefore, that we identify any impending problems facing deep FIR surveys with *Herschel*, particularly in the SPIRE bands (250–500  $\mu$ m) where Devlin et al. (2009) predict confusion limits only  $1.5\times$  lower than those suffered by BLAST.

#### 3.1 Radio identifications

The positional uncertainty of a source found in a map is given by

$$\sigma_{\text{pos}} = 0.6 [\text{SNR}^2 - (2\gamma + 4)]^{-1/2} \text{FWHM} \quad (1)$$

for a situation, where the counts obey a power law of the form  $N(>S) \propto S^{-\gamma}$  (Ivison et al. 2007b). The SNR term here is determined optimally in a beam-smoothed map and includes any variance due to confusion. The signal is uncorrected for flux boosting and the positional offset is not radial but is instead measured in right ascension or declination.

To associate radio emitters with the FIR sources in our sample, we utilize the technique of Downes et al. (1986), as implemented by Ivison et al. (2002) and by most FIR/submm identification work thereafter. According to Downes et al.,  $P$  is the probability of a random association and depends on the surface density of radio emitters and the radius within which one searches. The recent convention has been to accept associations as secure identifications where  $P < 0.05$ . We assume a slope of 1.5 for the radio counts in the relevant flux density regime ( $\sim 40$ – $400$   $\mu$ Jy) and fine-tune the absolute level of the counts with Monte Carlo simulations.

In choosing the search radius, we wish to maximize the number of secure, unambiguous identifications and to minimize the number of real counterparts missed. Fig. 3 illustrates how the total number of secure identifications and the integrated value of  $P$  for those sources [hereafter  $\Sigma P(P < 0.05)$ ] varies with choice of search radius.  $\Sigma P(P < 0.05)$  equates directly to the expected number of spurious identifications in the sample. It is not intuitively obvious why there is a well-defined peak in  $\Sigma P(P < 0.05)$  when the total number of secure identifications is roughly constant with search radius: we see this because faint, real radio identifications compete (in terms of low  $P$ ) with rare, bright sources – radio-loud AGN, entirely unrelated to the FIR source; as the search radius increases, correct identifications drop out of the integral (simply because their  $P$  rises above 0.05); the resulting reduction in secure identifications is balanced by radio-loud AGN – contaminants; since they are very bright, their  $P$  tends to zero as soon as they are within the search radius; thus  $\Sigma P(P < 0.05)$  drops gently while the number of apparently ‘secure’ identifications is maintained. Allowing a search radius well beyond that of the peak  $P$  is therefore not advisable.

We express the search radius in terms of multiples of  $\sigma_{\text{pos}}$  to maintain an appropriate dependence on the SNR of the source for which a counterpart is sought. Based on Fig. 3, we search within a radius of  $3\sigma_{\text{pos}}$ , though values as low as  $1.5\sigma_{\text{pos}}$  are defensible choices. This yields 12 statistically secure identifications with an expectation that  $\sim 0.24$  lie outside the search area (calculated via the cumulative Rayleigh distribution function).

At face value, the fraction of 250- $\mu$ m sources with secure radio identifications, 55 per cent, is similar to that found for SMGs (e.g. Smail et al. 2000; Ivison et al. 2002, 2007b; Pope et al. 2006), which are expected to have higher luminosities and higher redshifts (Chapman et al. 2005). However, close examination of Fig. 2, in which we have superimposed the radio and

<sup>3</sup>E-mail: rji@roe.ac.uk

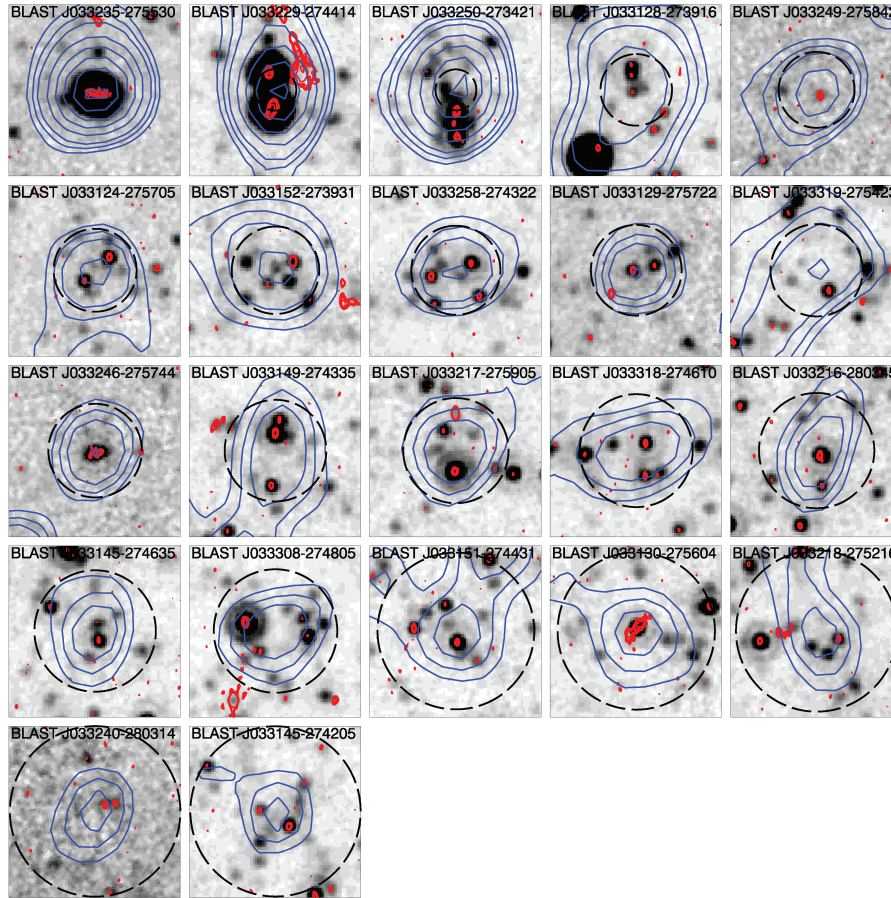


**Figure 2.** *Spitzer* 24- $\mu$ m grey-scale images superimposed with red 1400-MHz contours and blue 250- $\mu$ m contours, centred on BLAST 250- $\mu$ m-selected sources which are labelled with their names. Each postage stamp image is  $90 \times 90$  arcsec<sup>2</sup>. Dashed black circles show our search areas ( $3\sigma_{\text{pos}}$  radius – see Section 3). Broadly speaking, the sources are associated with either large spirals or clumps of faint, 24- $\mu$ m galaxies – sometimes several of the former or as many as seven of the latter. The number of double sources is striking, especially those where the 250- $\mu$ m emission peaks between the two.

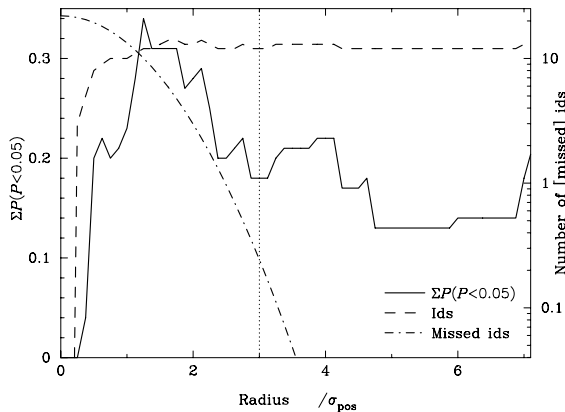


**Figure 3.** Illustration of how the integrated value of  $P$  for identifications with  $P < 0.05$  [so  $\Sigma P(P < 0.05)$ ] for our sample varies with choice of search radius, where search radius is in multiples of  $\sigma_{\text{pos}}$  (the rms offset between observed and actual coordinates in RA or Dec. – see equation 1). This is the solid line, and the left-hand axis. In a situation not dominated by the effects of confusion, the value at the chosen radius equates directly to the expected number of spurious identifications amongst our sample. The right-hand axis shows the total number of identifications in our sample, and the number that we would expect to miss by selecting too small a search radius. The dotted line shows the adopted search radius – in this case  $3\sigma_{\text{pos}}$  – where we have 12 formal identifications and  $\sim 0.24$  was likely to have fallen outside our search radius.

250- $\mu$ m data on a 24- $\mu$ m grey-scale image of each BLAST source, reveals that our ability to securely associate radio counterparts with FIR emitters has been compromised. Broadly speaking, the BLAST sources are associated with either large spirals or clumps of faint, radio and/or 24- $\mu$ m galaxies – sometimes several of the former or as many as seven of the latter (e.g. BLAST J033152–273931). At least half of the FIR sources appear to be blends of two or more faint galaxies – each often with faint radio identifications – i.e. confusion is a major problem (Condon 1974; Blain, Ivison & Smail 1998). This is compounded by the large number of radio sources found by chance in the required search area (a situation that worsens at 24  $\mu$ m, as mentioned earlier). Both issues are related to the relatively large size of the 250- $\mu$ m beam (and the situation is worse at 350 and 500  $\mu$ m).

As an alternative approach, we inspected the data shown in Fig. 2 by eye, rejecting seven sources with complicated 250- $\mu$ m morphologies suggestive of multiple, blended emitters. Of the remaining 15, nine have statistically secure radio identifications; of these, only three have unambiguous, single identifications. In total, therefore, only 14 per cent of our parent sample has secure, unambiguous radio identifications, based on this more subjective approach.

Thus, the purely statistical technique advocated previously for SMG identification work proves unhelpful – even misleading – in the confusion-dominated regime faced by BLAST and anticipated for the deepest survey work with *Herschel* (see Fig. 1



caption). Working through the *Spitzer* and Photodetector Array Camera and Spectrometer (PACS; Poglitsch et al. 2008) bands to identify the dominant contributors to SPIRE flux densities may be more fruitful – but this has yet to be tested. This argues that a stacking approach may be the most enlightening – we turn to this later.

### 3.2 24- $\mu\text{m}$ identifications

Using a different probabilistic approach to our own, Dye et al. (2009) listed the most likely 24- $\mu\text{m}$  counterparts for many of our 250- $\mu\text{m}$ -selected galaxies. To their list, we added BLAST J033229–274414, an obvious blend of two galaxies at  $z \sim 0.08$  (Fig. 2), and in a further six cases where Dye et al. listed no association we added the most likely of our own 24- $\mu\text{m}$  identifications. We list the 24- $\mu\text{m}$  positions in Table 1, together with the radio properties at those positions. The FIR and submm properties at the 24- $\mu\text{m}$  positions are given in Table 2.

As already noted, we adopt these 24- $\mu\text{m}$  counterparts to avoid introducing a strong radio-related bias, and despite the problems caused by the high surface density of 24- $\mu\text{m}$  emitters, exacerbated by FIR confusion.

## 4 RESULTS

### 4.1 Redshift distribution

Of the most likely 24- $\mu\text{m}$  counterparts for our 250- $\mu\text{m}$  sample, eight have spectroscopic redshifts (see Croom, Warren & Glazebrook 2001; Le Fèvre et al. 2004; Szokoly et al. 2004; Vanzella et al. 2008; Eales et al. 2009) and another 11 have photometric redshifts (Rafferty et al., in preparation). For every spectroscopic case, both types of estimate are available, and these agree reasonably well ( $\delta z_{\text{rms}} \lesssim 0.05$ , with one outlier). We were unable to assign redshifts with confidence in two cases (see Tables 1 and 2).

The redshift distribution of 24- $\mu\text{m}$ -identified, 250- $\mu\text{m}$ -selected sources is shown in Fig. 4. The median is  $z = 0.74$  with an interquartile range of  $z = 0.25$ – $1.57$ , so slightly beyond the 70- $\mu\text{m}$ -selected sample of Symeonidis et al. (2009) which had a median  $z$  of 0.42. Inset in the same plot is a histogram of  $S_{500\mu\text{m}}/S_{250\mu\text{m}}$ . This ratio should increase with redshift as the SED peak shifts to longer wavelengths, and we find a strong tendency for those above the median redshift to have higher ratios.

### 4.2 Far-infrared SEDs

Flux boosting of nearly the same magnitude as that experienced in the BLAST wavebands (Section 2.1) also influences our *Spitzer* measurements and, to a lesser extent, those made using LABOCA. We therefore apply deboosting factors appropriate for the BLAST 250- $\mu\text{m}$  sources – appropriate to the level of precision required (Eales et al. 2009) – to  $S_{\text{IR}}$ , which we define to be the flux observed between rest frame 8 and 1000  $\mu\text{m}$ . The large uncertainty in the deboosting factor is propagated in quadrature with other uncertainties.  $S_{\text{IR}}$  could be determined via modified blackbody fits to the 70-, 160-, 250-, 350-, 500- and 870- $\mu\text{m}$  flux measurements with  $\beta$  fixed to 1.5 (for example). However, with such well-sampled SEDs at our disposal, we concluded that  $S_{\text{IR}}$  is better determined by interpolating between the measured flux densities at 24–870  $\mu\text{m}$ , and extrapolating outside the data range to rest frame 8 and 1000  $\mu\text{m}$  with spectral indices of  $-1.8$  (appropriate for an M82-like SED) and  $+3.5$ , respectively, then deboosting according to the recipe in

Eales et al. (2009). These are the values listed in Table 2. Fig. 5 shows the deboosted IR luminosity as a function of redshift for our sample.

We do use modified blackbody fits to estimate the effective dust temperature,  $T_d$ , and these are also presented in Table 2. We note that several dust components with a range of temperatures would be required to replicate the SEDs accurately over the full wavelength range. The average observed-frame  $T_d$  is  $20.5 \pm 3.5$  K. Fig. 6 shows the relationship between rest-frame  $T_d$  and  $L_{\text{IR}}$ . We expect and see a strong correlation, following the work by Dunne et al. (2000) and Chapman et al. (2005): at 250  $\mu\text{m}$ , we are sensitive to a particular observed temperature regime; rest-frame  $T_d$  is higher (by a factor  $1+z$ ) than observed  $T_d$ , so for more distant detected sources we expect hotter dust.  $L_{\text{IR}}$  scales with a high power of  $T_d$ , yielding the strong correlation evident in Fig. 6.

### 4.3 The FIR/radio correlation

We have explored trends in the FIR/radio correlation, both the monochromatic version, e.g.  $q_{70} = \log_{10}(S_{70\mu\text{m}}/S_{1400\text{MHz}})$  as defined by Appleton et al. (2004) – where  $K$ -correcting both  $S_{70\mu\text{m}}$  and  $S_{1400\text{MHz}}$  requires assumptions about SED shape if a significant range of redshift is present – and the correlation between bolometric  $S_{\text{IR}}$  and  $K$ -corrected radio flux density, where both quantities are well constrained.

We adopt a standard routine so that we can compare like with like. First, we exclude a radio-loud AGN, identified on the basis of its radio morphology (BLAST J033130–275604). We do not exclude the X-ray emitters (see Table 1). Next, we calculate the error-weighted mean and standard deviation of the relevant  $q$  parameter, noting points that deviate from the mean by more than  $3\sigma$  (these being ‘radio-excess AGN’ candidates, as described by Donley et al. 2005). The resultant statistics (and notes) are reported in Table 3.

#### 4.3.1 Monochromatic correlations

The monochromatic relationship between  $S_{250\mu\text{m}}$  and  $S_{1400\text{MHz}}$ ,  $q_{250} = \log_{10}(S_{250\mu\text{m}}/S_{1400\text{MHz}})$  is shown in Fig. 7 as a function of redshift, and the resultant statistics are reported in Table 3. Also shown as a grey box in Fig. 7 is the  $\pm 1\sigma$  range of  $q_{160}$  measured for the 57 members of the *Spitzer* IR Nearby Galaxies Survey (SINGS) sample which are detected at both 160  $\mu\text{m}$  and 1400 MHz (Dale et al. 2007). At  $z \approx 0.6$ , where the BLAST 250- $\mu\text{m}$  filter samples rest-frame 160- $\mu\text{m}$  emission, values of  $q_{160}$  and  $q_{250}$  are entirely compatible with the SINGS average, with or without the small radio  $K$ -correction. We interpret this as evidence for a low rate of evolution, at least out to  $z \sim 0.6$ .

#### 4.3.2 $K$ -corrected monochromatic correlations

Next, we looked at the effect of ‘ $K$ -correcting’ the monochromatic relationship between 250- $\mu\text{m}$  and 1400-MHz flux densities, where  $K$  is the function that transforms a quantity observed at some frequency into an equivalent measurement in the rest frame of the source being observed. Taking the simple case of a power-law SED, where  $L_v^K$  and  $S_v^{\text{obs}}$  are the  $K$ -corrected luminosity density and observed flux density, respectively, and  $d_{\text{lum}}$  is the luminosity distance (in m),

$$L_v^K = \frac{4\pi d_{\text{lum}}^2}{(1+z)} K S_v^{\text{obs}}, \quad (2)$$

**Table 2.** FIR–submm photometry at the positions of the 24- $\mu$ m identifications, prior to deboosting, plus radio luminosities, temperatures and adopted redshifts.

| Name                 | $S_{70\mu\text{m}}/\text{mJy}$ | $S_{160\mu\text{m}}/\text{mJy}$ | $S_{250\mu\text{m}}/\text{mJy}$ | $S_{350\mu\text{m}}/\text{mJy}$ | $S_{500\mu\text{m}}/\text{mJy}$ | $S_{870\mu\text{m}}/\text{mJy}$ | $T_d$ (obs)/<br>$\text{K}$           | $S_{\text{IR}}/10^{-15} \text{ W m}^{-2}$ | $L_{1400\text{MHz}}^\alpha/\text{W Hz}^{-1}$ | Adopted<br>$z$ |
|----------------------|--------------------------------|---------------------------------|---------------------------------|---------------------------------|---------------------------------|---------------------------------|--------------------------------------|---|--|----------------|
| BLAST J033235–275530 | 93.9 $\pm$ 11.2                | 351.1 $\pm$ 65.0                | 176.8 $\pm$ 10.9                | 75.4 $\pm$ 8.6                  | 29.8 $\pm$ 6.0                  | 1.23 $\pm$ 1.16                 | 25.2 <sup>+0.7</sup> <sub>-0.9</sub> | 8.28 $\pm$ 1.79                           | 2.18 $\times$ 10 <sup>21</sup>               | 0.038          |
| BLAST J033229–274414 | 136.6 $\pm$ 15.4               | 368.0 $\pm$ 65.8                | 141.6 $\pm$ 10.8                | 71.7 $\pm$ 8.5                  | 36.8 $\pm$ 6.0                  | 0.88 $\pm$ 1.17                 | 27.2 <sup>+0.9</sup> <sub>-1.0</sub> | 10.5 $\pm$ 2.8                            | 2.13 $\times$ 10 <sup>22</sup>               | 0.077          |
| BLAST J033250–273421 | 30.1 $\pm$ 4.9                 | 203.5 $\pm$ 43.1                | 154.8 $\pm$ 11.0                | 76.9 $\pm$ 8.7                  | 40.3 $\pm$ 6.0                  | 1.82 $\pm$ 1.22                 | 21.5 <sup>+0.5</sup> <sub>-0.9</sub> | 4.22 $\pm$ 1.24                           | 8.45 $\times$ 10 <sup>22</sup>               | 0.251          |
| BLAST J033128–273916 | 7.1 $\pm$ 1.9                  | 88.5 $\pm$ 25.2                 | 105.3 $\pm$ 11.1                | 69.6 $\pm$ 8.7                  | 39.8 $\pm$ 6.3                  | 4.02 $\pm$ 1.18                 | 18.1 <sup>+0.6</sup> <sub>-0.8</sub> | —   | —  | —              |
| BLAST J033249–275842 | 8.4 $\pm$ 2.1                  | 72.6 $\pm$ 21.7                 | 101.2 $\pm$ 10.9                | 66.4 $\pm$ 8.6                  | 22.6 $\pm$ 6.0                  | 1.75 $\pm$ 1.13                 | 19.3 <sup>+0.7</sup> <sub>-1.0</sub> | 1.28 $\pm$ 0.63                           | 6.38 $\times$ 10 <sup>24</sup>               | 2.215          |
| BLAST J033124–275705 | 8.7 $\pm$ 2.3                  | 100.7 $\pm$ 30.1                | 83.2 $\pm$ 11.1                 | 47.2 $\pm$ 8.7                  | 33.3 $\pm$ 6.2                  | 2.99 $\pm$ 1.20                 | 19.0 <sup>+0.7</sup> <sub>-0.9</sub> | 1.40 $\pm$ 0.70                           | 7.07 $\times$ 10 <sup>24</sup>               | 2.732          |
| BLAST J033152–273931 | 3.0 $\pm$ 1.4                  | 31.9 $\pm$ 14.4                 | 78.3 $\pm$ 11.0                 | 64.3 $\pm$ 8.6                  | 53.1 $\pm$ 6.0                  | 3.49 $\pm$ 1.14                 | 15.9 <sup>+1.7</sup> <sub>-1.8</sub> | 0.77 $\pm$ 0.42                           | 2.35 $\times$ 10 <sup>25</sup>               | 2.296          |
| BLAST J033258–274322 | 7.4 $\pm$ 2.0                  | 82.8 $\pm$ 24.8                 | 71.5 $\pm$ 11.1                 | 53.6 $\pm$ 8.7                  | 34.3 $\pm$ 6.0                  | 4.31 $\pm$ 1.17                 | 18.3 <sup>+0.7</sup> <sub>-0.9</sub> | 1.21 $\pm$ 0.61                           | 9.48 $\times$ 10 <sup>23</sup>               | 1.160          |
| BLAST J033129–275722 | 3.6 $\pm$ 1.7                  | 49.0 $\pm$ 19.9                 | 91.6 $\pm$ 11.0                 | 54.4 $\pm$ 8.7                  | 46.3 $\pm$ 6.2                  | 5.11 $\pm$ 1.14                 | 16.1 <sup>+1.4</sup> <sub>-1.0</sub> | 0.93 $\pm$ 0.49                           | 1.78 $\times$ 10 <sup>24</sup>               | 1.571          |
| BLAST J033319–275423 | 3.9 $\pm$ 1.4                  | 36.0 $\pm$ 14.9                 | 84.2 $\pm$ 11.0                 | 20.4 $\pm$ 8.5                  | 13.2 $\pm$ 5.9                  | 1.12 $\pm$ 1.13                 | 18.8 <sup>+1.2</sup> <sub>-1.4</sub> | 0.71 $\pm$ 0.41                           | 5.24 $\times$ 10 <sup>22</sup>               | 0.488          |
| BLAST J033246–275744 | 46.0 $\pm$ 6.0                 | 147.9 $\pm$ 32.9                | 90.0 $\pm$ 10.9                 | 46.7 $\pm$ 8.5                  | 18.7 $\pm$ 5.9                  | 1.30 $\pm$ 1.14                 | 24.3 <sup>+1.0</sup> <sub>-1.0</sub> | 3.03 $\pm$ 1.34                           | 8.49 $\times$ 10 <sup>21</sup>               | 0.103          |
| BLAST J033149–274335 | 15.7 $\pm$ 2.8                 | 100.5 $\pm$ 24.3                | 81.5 $\pm$ 11.0                 | 46.6 $\pm$ 8.6                  | 30.9 $\pm$ 5.9                  | 2.46 $\pm$ 1.16                 | 20.7 <sup>+0.8</sup> <sub>-1.0</sub> | 1.51 $\pm$ 0.79                           | 2.75 $\times$ 10 <sup>23</sup>               | 0.618          |
| BLAST J033217–275905 | 39.5 $\pm$ 5.9                 | 110.4 $\pm$ 30.4                | 80.5 $\pm$ 11.0                 | 63.6 $\pm$ 8.5                  | 30.4 $\pm$ 6.0                  | 1.62 $\pm$ 1.14                 | 23.9 <sup>+1.1</sup> <sub>-1.1</sub> | 2.00 $\pm$ 1.04                           | 7.17 $\times$ 10 <sup>21</sup>               | 0.126          |
| BLAST J033318–274610 | 5.6 $\pm$ 1.7                  | 62.3 $\pm$ 20.8                 | 79.9 $\pm$ 10.8                 | 72.5 $\pm$ 8.6                  | 51.4 $\pm$ 5.9                  | 3.84 $\pm$ 1.13                 | 17.7 <sup>+0.8</sup> <sub>-0.9</sub> | 1.00 $\pm$ 0.56                           | 2.94 $\times$ 10 <sup>24</sup>               | 2.059          |
| BLAST J033216–280345 | 16.0 $\pm$ 3.2                 | 85.7 $\pm$ 24.5                 | 82.1 $\pm$ 11.0                 | 39.2 $\pm$ 8.5                  | –0.3 $\pm$ 6.0                  | 2.04 $\pm$ 1.30                 | 21.2 <sup>+1.0</sup> <sub>-1.1</sub> | 1.31 $\pm$ 0.70                           | 1.31 $\times$ 10 <sup>23</sup>               | 0.452          |
| BLAST J033145–274635 | –0.3 $\pm$ 1.0                 | 12.0 $\pm$ 10.4                 | 75.2 $\pm$ 10.8                 | 11.0 $\pm$ 8.5                  | 12.8 $\pm$ 5.9                  | 0.30 $\pm$ 1.14                 | 15.2 <sup>+1.1</sup> <sub>-1.7</sub> | —   | —  | —              |
| BLAST J033308–274805 | 53.0 $\pm$ 6.6                 | 97.9 $\pm$ 26.6                 | 66.1 $\pm$ 10.8                 | 37.0 $\pm$ 8.5                  | 31.7 $\pm$ 5.9                  | 2.02 $\pm$ 1.16                 | 25.9 <sup>+1.3</sup> <sub>-1.5</sub> | 1.99 $\pm$ 1.04                           | 3.65 $\times$ 10 <sup>22</sup>               | 0.180          |
| BLAST J033151–274431 | 6.0 $\pm$ 1.7                  | 77.5 $\pm$ 20.2                 | 74.0 $\pm$ 10.8                 | 63.8 $\pm$ 8.5                  | 37.4 $\pm$ 5.9                  | 4.18 $\pm$ 1.16                 | 17.9 <sup>+0.7</sup> <sub>-0.9</sub> | 1.05 $\pm$ 0.61                           | 2.13 $\times$ 10 <sup>24</sup>               | 1.911          |
| BLAST J033130–275604 | 28.5 $\pm$ 4.1                 | 83.2 $\pm$ 24.7                 | 74.0 $\pm$ 10.8                 | 20.9 $\pm$ 8.5                  | 44.9 $\pm$ 6.0                  | 3.05 $\pm$ 1.15                 | 23.0 <sup>+1.1</sup> <sub>-1.2</sub> | 1.61 $\pm$ 0.91                           | 2.10 $\times$ 10 <sup>24</sup>               | 0.677          |
| BLAST J033218–275216 | 5.3 $\pm$ 1.4                  | 54.2 $\pm$ 17.8                 | 71.4 $\pm$ 10.8                 | 52.6 $\pm$ 8.5                  | 46.8 $\pm$ 5.9                  | 7.74 $\pm$ 1.17                 | 16.1 <sup>+2.3</sup> <sub>-1.1</sub> | 0.88 $\pm$ 0.52                           | 5.63 $\times$ 10 <sup>22</sup>               | 0.739          |
| BLAST J033240–280314 | 6.8 $\pm$ 2.0                  | 50.7 $\pm$ 18.6                 | 72.7 $\pm$ 11.0                 | 61.8 $\pm$ 8.5                  | 30.6 $\pm$ 6.1                  | 4.05 $\pm$ 1.25                 | 18.2 <sup>+1.4</sup> <sub>-1.4</sub> | 0.90 $\pm$ 0.54                           | 9.53 $\times$ 10 <sup>23</sup>               | 0.956          |
| BLAST J033145–274205 | 4.8 $\pm$ 1.6                  | 45.0 $\pm$ 17.2                 | 56.0 $\pm$ 11.0                 | 27.0 $\pm$ 8.7                  | 28.4 $\pm$ 6.2                  | 1.98 $\pm$ 1.14                 | 18.8 <sup>+1.0</sup> <sub>-1.5</sub> | 0.70 $\pm$ 0.45                           | 6.38 $\times$ 10 <sup>23</sup>               | 1.056          |

Notes:  $-L_{1400\text{MHz}}^\alpha$  is the  $K$ -corrected radio luminosity using the measured  $\alpha$ .  $S_{\text{IR}}$  is deboosted; this process dominates the error budget (see Sections 2.1 and 4.2). Spectroscopic redshifts are shown in italics.



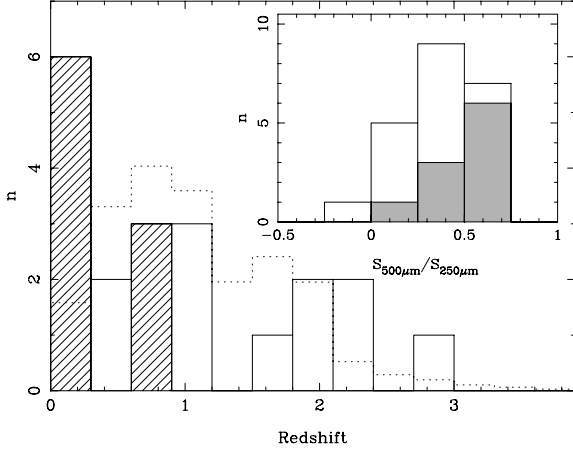


**Figure 4.** The redshift distribution of the most likely 24- $\mu$ m associations with our BLAST 250- $\mu$ m sample. The dotted line shows the redshift distribution of the 24- $\mu$ m sources used for stacking in Section 4.4. The subset of galaxies with spectroscopic redshifts is shown as a hatched area. Inset is a histogram of  $S_{500\mu\text{m}}/S_{250\mu\text{m}}$ , where we expect galaxies at higher redshifts to have higher ratios. Sources at redshifts higher than the median ( $z = 0.74$ ) are shaded and there is a very clear tendency for these to have higher ratios, as we would expect.

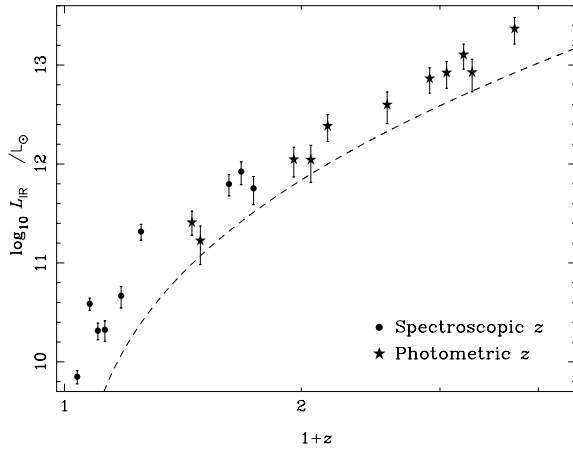


**Figure 5.** Deboosted IR luminosity as a function of redshift. The dashed line is an arbitrarily scaled detection threshold for our adopted cosmology. Galaxies with spectroscopic and photometric redshifts are plotted as circles and stars, respectively.

where the  $(1+z)$  term takes care of the extra width of the differential frequency element in the observed frame. Now imagine we are working on a sample of  $z = 1$  galaxies at 1400 MHz: the factor  $K$  converts  $S_{1400\text{MHz}}^{\text{obs}}$  – radiation emitted at 2800 MHz and seen at 1400 MHz – into  $S_{1400\text{MHz}}^K$ , the 1400-MHz flux density in the rest frame of the emitter. Using the definitions of  $z$  and spectral index,  $\alpha$ , i.e.  $(1+z) = \nu_{\text{rest}}/\nu_{\text{obs}}$  and  $S_\nu \propto \nu^\alpha$ , we find that  $K = S_\nu^K/S_\nu^{\text{obs}} = (1+z)^{-\alpha}$ , so

$$L_\nu^K = \frac{4\pi d_{\text{lum}}^2}{(1+z)} S_\nu^{\text{obs}} (1+z)^{-\alpha} = 4\pi d_{\text{lum}}^2 \frac{S_\nu^{\text{obs}}}{(1+z)^{1+\alpha}}. \quad (3)$$

For the radio spectrum, we use the measured slope between 610 and 1400 MHz, adopting  $\alpha = -0.8$ , where this is consistent with the 610-MHz upper limit or where no measurement is available. This results in a median  $\alpha$  of  $-0.4$ . In the FIR waveband, we explored two options. One is to adopt the observed SED of M82, which Ibar et al. (2008) found gave the least scatter in  $q_{24}$ .  $K$ -

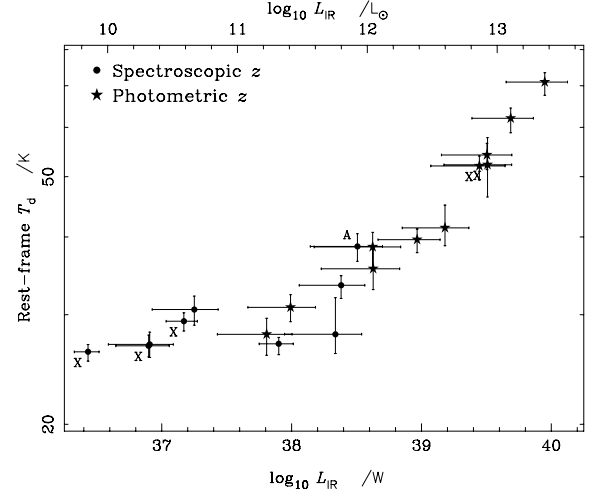


**Figure 6.**  $T_d$  versus deboosted IR luminosity. Galaxies with spectroscopic and photometric redshifts are plotted as circles and stars, respectively. A radio-loud AGN, selected via its radio morphology, is labelled ‘A’; X-ray emitters are labelled ‘X’. The strong correlation between  $T_d$  and  $L_{60\mu\text{m}}$  seen by Dunne et al. (2000) is also evident here. Selection at 250  $\mu$ m tends to find local galaxies with  $T_d \approx 20$  K, but inevitably also catches more luminous, distant galaxies with the same *observed*  $T_d$  and *rest-frame* values of  $T_d$  that are  $\approx (1+z)\times$  higher.

corrections<sup>4</sup> appropriate for an M82 SED template in the *Spitzer*, BLAST and LABOCA wavebands, calculated using accurate filter transmission profiles, are shown in Fig. 8. We also tried the SED of Arp 220 and an SED built from those 250- $\mu$ m-selected galaxies with secure identifications and redshifts, normalized at 250  $\mu$ m using the technique of Pope et al. (2006) – see Fig. 9. The latter SED made an appreciable difference to the absolute value of  $q_{250}$  and resulted in less scatter. Relevant statistics for  $q_{250}$  under each set of assumptions are reported in Table 3.

#### 4.3.3 $K$ -corrected bolometric correlations

Moving from the monochromatic correlation to bolometric quantities, where a  $K$ -correction is required only in the radio waveband. Helou et al. (1985) defined  $q_{\text{IR}}$  such that

$$q_{\text{IR}} = \log \left( \frac{S_{\text{FIR}}/3.75 \times 10^{12}}{W \text{ m}^{-2}} \right) - \log \left( \frac{S_{1400\text{MHz}}}{W \text{ m}^{-2} \text{ Hz}^{-1}} \right), \quad (4)$$

where they defined  $S_{\text{FIR}}$  as the flux between 42.5 and 122.5  $\mu$ m and  $3.75 \times 10^{12}$  is the frequency at their mid-band, 80  $\mu$ m. Working at 42.5–122.5  $\mu$ m would exploit only one-tenth of the wavelength coverage now at our disposal so, although we adopt this definition, we use  $S_{\text{IR}}$  – the flux between rest frame 8 and 1000  $\mu$ m – instead of  $S_{\text{FIR}}$ .

We  $K$ -correct the radio flux densities as described in the discussion of monochromatic relations. The results are shown in Fig. 10 and reported in Table 3. Utilizing all the data at our disposal, we find  $q_{\text{IR}} = 2.41 \pm 0.20$  for our 250- $\mu$ m-selected galaxy sample, with no evidence of redshift dependence.

<sup>4</sup>Our IDL-based  $K$ -correction code, together with SED templates and filter profiles, is available on request.

**Table 3.** Summary of  $q$  statistics.

| Type of $q$   | Mean        | Standard deviation | $K$ -correction(s) or stacking parameters             |
|---|-------------|--------------------|---|
| 250- $\mu$ m-selected galaxy sample:                      |             |                    |   |
| $q_{250}$   | 2.26        | 0.35               | None  |
| $q_{250}$   | 1.85*       | 0.43               | M82 SED, $\alpha = -0.8$                              |
| $q_{250}$   | 1.82*       | 0.43               | Arp 220 SED, $\alpha = -0.8$                          |
| $q_{250}$   | 2.08        | 0.34               | Fig. 9 SED, $\alpha = -0.8$                           |
| $q_{250}$   | 1.94        | 0.34               | M82 SED, measured $\alpha$                            |
| $q_{250}$   | 1.91        | 0.34               | Arp 220 SED, measured $\alpha$                        |
| $q_{250}$   | <b>2.18</b> | <b>0.28</b>        | Fig. 9 SED, measured $\alpha$                         |
| $q_{\text{IR}}$   | 2.40        | 0.29               | None  |
| $q_{\text{IR}}$   | 2.37        | 0.31               | $\alpha = -0.8$                                       |
| $q_{\text{IR}}$   | <b>2.41</b> | <b>0.20</b>        | Measured $\alpha$                                     |
| SINGS sample (Dale et al. 2007):                          |             |                    |   |
| $q_{160}$   | 2.68        | 0.41               | None  |
| Stacking on 24- $\mu$ m-selected galaxies:                |             |                    |   |
| $q_{250}$   | 2.70        | 0.08               | None  |
| $q_{250}$   | 2.00        | 0.37               | M82 SED, measured $\alpha$                            |
| $q_{250}$   | 2.31        | 0.18               | Fig. 9 SED, measured $\alpha$                         |
| $q_{\text{IR}}$   | 2.89        | 0.06               | None  |
| $q_{\text{IR}}$   | 2.67        | 0.17               | Measured $\alpha$                                     |
| Stacking on radio-selected galaxies (no $K$ -correction): |             |                    |   |
| $q_{250}$   | 2.05        | 0.34               | Measured $\alpha$                                     |
| $q_{250}$   | 2.42        | –                  | $40 < S_{1400 \text{ MHz}} < 100 \mu\text{Jy}$ [507]  |
| $q_{250}$   | 2.17        | –                  | $100 < S_{1400 \text{ MHz}} < 251 \mu\text{Jy}$ [224] |
| $q_{250}$   | 1.81        | –                  | $251 < S_{1400 \text{ MHz}} < 631 \mu\text{Jy}$ [69]  |
| $q_{250}$   | 1.56        | –                  | $631 < S_{1400 \text{ MHz}} < 1000 \mu\text{Jy}$ [16] |
| $q_{\text{IR}}$   | 1.96        | 0.34               | Measured $\alpha$                                     |
| $q_{\text{IR}}$   | 2.25        | –                  | $40 < S_{1400 \text{ MHz}} < 100 \mu\text{Jy}$ [507]  |
| $q_{\text{IR}}$   | 2.11        | –                  | $100 < S_{1400 \text{ MHz}} < 251 \mu\text{Jy}$ [224] |
| $q_{\text{IR}}$   | 1.87        | –                  | $251 < S_{1400 \text{ MHz}} < 631 \mu\text{Jy}$ [69]  |
| $q_{\text{IR}}$   | 1.29        | –                  | $631 < S_{1400 \text{ MHz}} < 1000 \mu\text{Jy}$ [16] |

† With M82-like power-law SED ( $\alpha = -1.8$ ) shortward of the peak.

\* One radio-excess AGN present.

#### 4.4 Assessing redshift evolution of the FIR/radio correlation by stacking

Marsden et al. (2009), Pascale et al. (2009) and Patanchon et al. (2009) have demonstrated the power of stacking analyses based on confusion-limited maps and the very steep BLAST source counts. We have applied those same techniques to study the evolution of  $q_{250}$  and  $q_{\text{IR}}$  by stacking at the positions of the thousands of mid-IR-selected galaxies with photometric redshifts in ECDFS. We thus eliminate the biases introduced by starting from a flux-boosted and confused FIR-selected sample and the problems of demanding secure identifications in a densely populated 24- $\mu$ m image. Since Marsden et al. (2009) have shown that the BLAST catalogue only comprises  $\approx 10$  per cent of the total flux in the maps, stacking, which uses all of the pixels, has the potential to greatly increase the sensitivity of the analysis.

However, some new problems are introduced. We have to worry about selection effects due to the catalogue of positions upon which we stack – in this case a 24- $\mu$ m-selected sample, with flux densities determined using Infrared Array Camera (IRAC) positions as priors (Magnelli et al. 2009), with the redshift distribution shown in Fig. 4 and with a non-trivial  $K$ -correction (see Fig. 8). Section 5 of Pascale et al. (2009) provides a practical demonstration of the paradigm described by Marsden et al. (2009) and shows that our fundamental

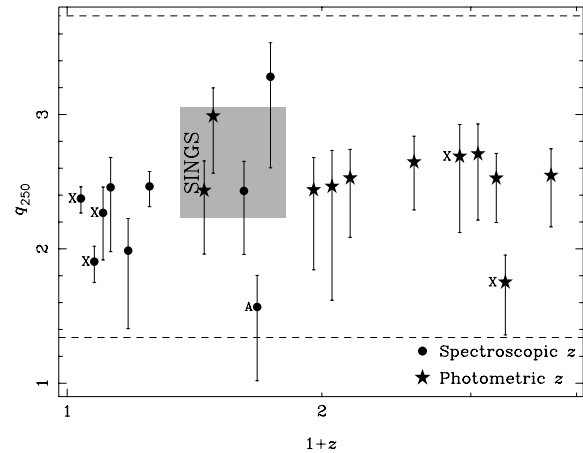


**Figure 7.**  $q_{250}$  versus redshift, where no  $K$ -corrections have been applied. Circles and stars represent spectroscopic and photometric redshifts, respectively. A radio-loud AGN, selected via its radio morphology, is labelled ‘A’; X-ray emitters are labelled ‘X’. The shaded region (around  $z \sim 0.56 \pm 0.20$ , where  $\lambda_{\text{rest}} = 160 \mu\text{m}$  for the BLAST 250- $\mu$ m filter) represents the  $\pm\sigma$  range of  $q_{160}$  measured for SINGS (Dale et al. 2007). A minor correction has been made to  $q_{160}$  ( $-0.04$ ) to emulate the effect of  $K$ -correcting the  $z = 0.56$  radio flux density for the BLAST sample.  $\pm 3\sigma$  deviations from the mean value of  $q_{250}$  are shown by dashed lines.

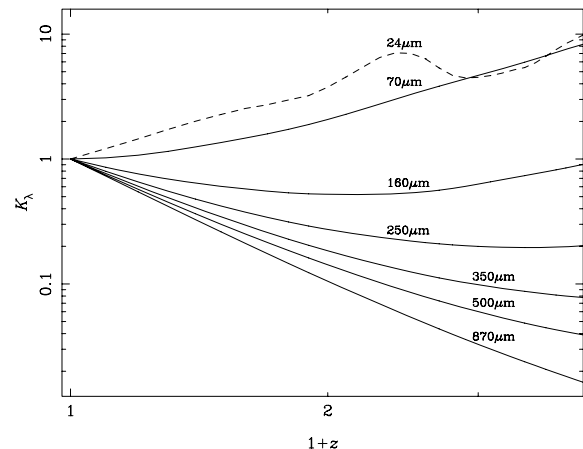


**Figure 8.**  $K$  corrections for the *Spitzer*, BLAST and LABOCA wavebands, assuming an M82 SED template, calculated using accurate filter transmission profiles and defined such that  $K = S_v^K / S_v^{\text{obs}}$ , so excluding the  $(1+z)$  term that takes care of the extra width of the differential frequency element in the observed frame (equation 2).

approach to stacking is accurate to the level of precision required here.

Median-stacking in the radio regime should reduce the consequences of radio-loud AGN becoming more prevalent at high redshift (Dunlop & Peacock 1990). Stacking should, therefore, allow us to probe the evolution of  $q$  for galaxies more representative of the general population than is possible for a sample requiring both FIR and radio detections, modulo 24- $\mu$ m selection biases.

We adopt the technique of Ivison et al. (2007a), dividing the Magnelli et al. catalogue into six redshift bins, evenly spaced in  $\log_{10}(1+z)$  between  $z=0$  and 3, containing 561, 1441, 2205, 1823, 1900 and 372 galaxies, respectively. Error-weighted mean postage-stamp images are obtained in all the FIR filters, allowing us to assess the level of any background emission. Median images are made from

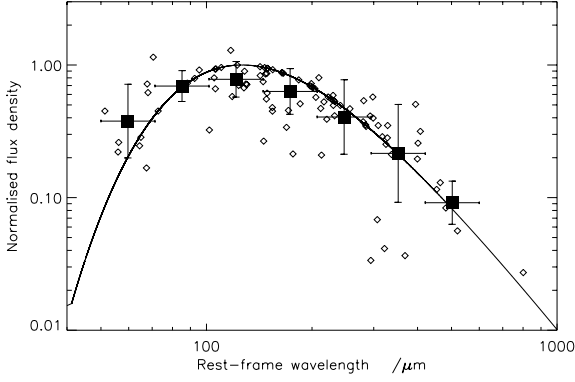


**Figure 9.** Template SED with arbitrary flux scale built from the normalized photometry of those 250- $\mu\text{m}$ -selected galaxies with secure identifications using the technique described by Pope et al. (2006). The solid line is a 36-K modified blackbody. To create a template from this SED, suitable for use in a  $K$ -correction algorithm, we interpolated between the means then extrapolated to shorter and longer wavelengths with  $\alpha = -1.8$  and  $+2.25$ , respectively.

the VLA and GMRT stacks, to reduce the influence of radio-loud AGN. In the radio regime, where the spatial resolution is relatively high, making images allows us to conserve flux density that would otherwise be lost due to smearing by astrometric uncertainties and finite bandwidth (chromatic aberration) at the cost of larger flux density uncertainties. Total flux densities are measured using Gaussian fits within *aips*; we determine the appropriate source centroid and width by making radio stacks using every available 24- $\mu\text{m}$  source ( $\text{SNR} \sim 50$ ), then fix these parameters to minimize flux density uncertainties and avoid spurious fits; at 1400 MHz, where both forms of smearing are most prevalent, flux densities were  $\sim 2\times$  higher than the peak values. Such losses are not expected where the astrometry is accurate to a small fraction of a beam, as it is at 70–870  $\mu\text{m}$ .

The *top* and *middle* panels of Fig. 11 show the evolution with redshift of the overall SED and the median radio spectral index,  $\alpha$ , for the Magnelli et al. (2009) sample. We see that the rest-frame 8–100- $\mu\text{m}$  portion of the SED becomes progressively more important – in terms of its relative contribution to  $S_{\text{IR}}$  – as we move to higher redshifts, despite the 870- $\mu\text{m}$  flux density increasing slightly with redshift (as expected – Blain & Longair 1993). We find no evidence of significant deviations from the error-weighted mean spectral index,  $\alpha_{610}^{1400} = -0.75 \pm 0.06$ , nor of a significant trend in  $\alpha_{610}^{1400}$  across  $0 < z < 3$ . A weighted least-squares fit yields  $\alpha_{610}^{1400} \propto (1+z)^{0.14 \pm 0.20}$ .

The lower panel of Fig. 11 shows the evolution with redshift of  $q_{250}$  and  $q_{\text{IR}}$ , the former  $K$ -corrected using the SED template described in Section 4.3 and shown in Fig. 9, both  $K$ -corrected using measured radio spectra. Mean values of both  $q_{250}$  and  $q_{\text{IR}}$  lie within  $1\sigma$  of the mean values found for our 250- $\mu\text{m}$ -selected galaxies (Table 3). We find, however, that  $q_{\text{IR}}$  evolves with redshift, even across  $0 < z < 1$  where incompleteness should not be a major issue in our 24- $\mu\text{m}$  sample. A weighted least-squares fit suggests  $q_{\text{IR}} \propto (1+z)^{-0.15 \pm 0.03}$ .  $q_{250}$  is also found to evolve, though the form of the evolution is strongly dependent on the choice of SED adopted for  $K$  correction, i.e. on the shape of the template SED shortward of 200  $\mu\text{m}$ , emphasising the importance of good spectral coverage. The evolution is even stronger for M82 and Arp 220 SEDs. The different behaviour with respect to redshift seen in Figs 10 and 11 is presumably due to selection biases: the lack of evolution seen

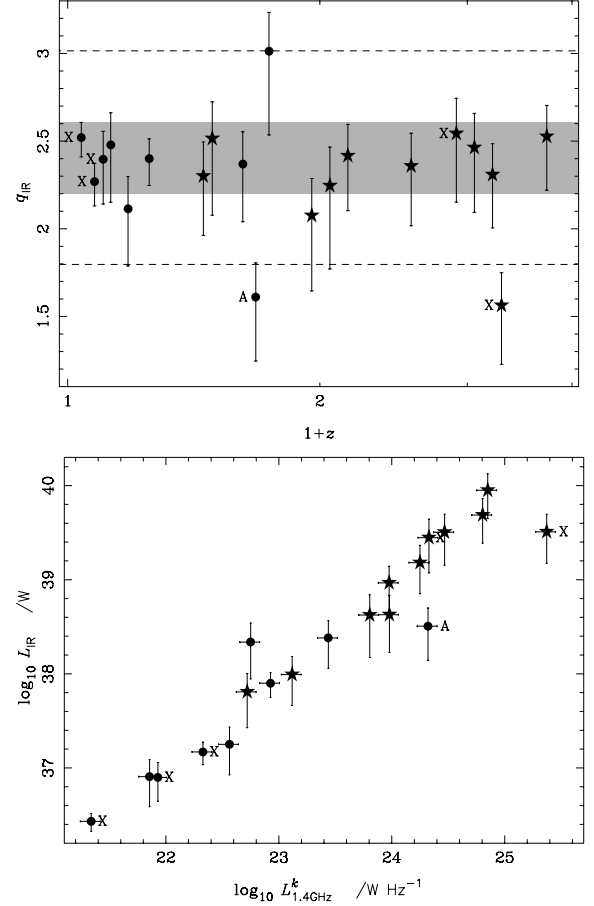


**Figure 10.** Upper:  $q_{\text{IR}}$  as a function of redshift, using  $K$ -corrected radio luminosities based on measured radio spectra. The shaded area represents  $\pm\sigma$ ; dashed lines are at  $\pm 3\sigma$ . Lower:  $L_{\text{IR}}$  versus  $L_{1400\text{MHz}}^\alpha$ . A radio-loud AGN, selected via its radio morphology, is labelled ‘A’; X-ray emitters are labelled ‘X’.

in Fig. 10 reflects the FIR sample selection employed there; the evolution seen in Fig. 11 reflects the IR and radio characteristics of the increasingly luminous 24- $\mu\text{m}$  emitters upon which we are stacking at progressively higher redshifts.

The use of *median* radio images should exclude radio-loud AGN at least as effectively as the  $3\sigma$  clip employed in Section 4.3, so the influence of the anticipated evolution (with redshift) of radio-loud AGN on the stacked values of  $q$  should be minimized. Using means instead, which we view as an inferior approach, the average spectral index,  $\alpha_{610}^{1400}$ , falls to  $-1.12$  as would be expected if steep-spectrum AGN contaminate the stacks. This, together with the  $\sim 3\times$  higher mean radio flux densities, shifts  $q_{\text{IR}}$  by  $-0.67$ , although the form of the redshift evolution remains similar, with  $q_{\text{IR}} \propto (1+z)^{-0.14 \pm 0.04}$ .

Responding to reports that the radio background is significantly brighter than the cumulative intensity seen in discrete radio emitters (Fixsen et al. 2009; Seiffert et al. 2009), Singal et al. (2009) have speculated that we should see the FIR/radio correlation evolve, driven by  $\sim 0.01$ – $10$ - $\mu\text{Jy}$  radio activity amongst ordinary star-forming galaxies. Since this is the flux density regime we are probing with our stacking analysis, one might hope to catch a glimpse of such evolution. Indeed, the basic form of the evolution we see in  $q_{\text{IR}}$  is consistent with the idea of Singal et al., and our spectral index is consistent with that of the radio background ( $\alpha_{22}^{8,000} \sim -0.6$ ; Fixsen et al. 2009).

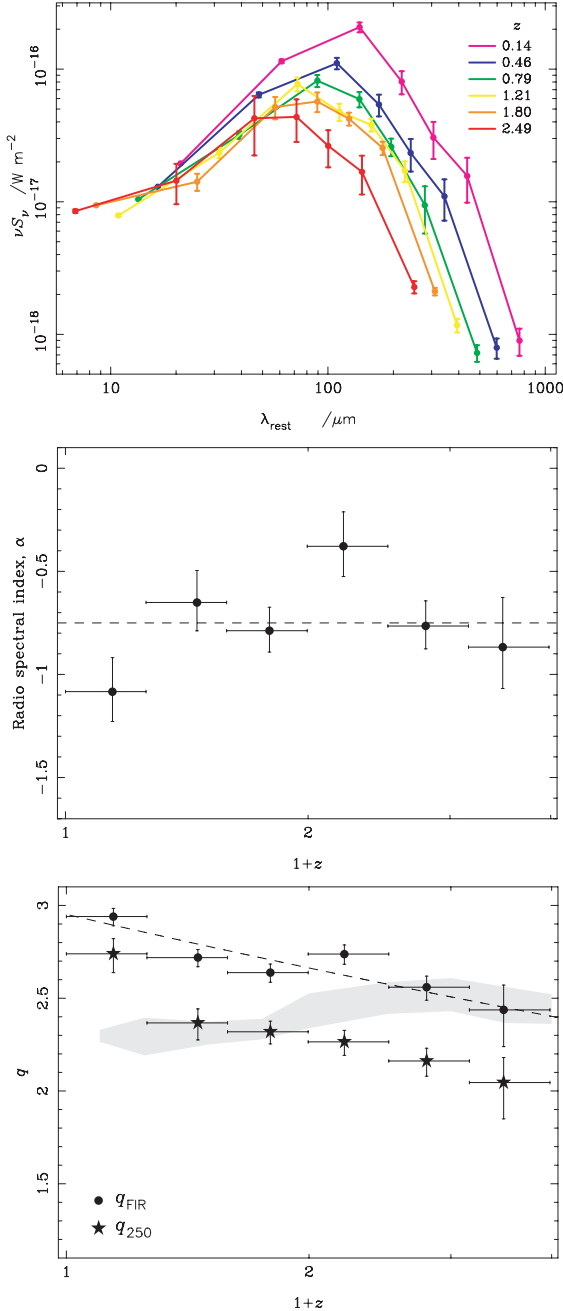


**Figure 11.** Top:  $\nu_{\text{obs}} S_{\nu_{\text{obs}}}$  versus rest wavelength in six redshift bins, measured at the positions of the 24- $\mu\text{m}$  sample (Magnelli et al. 2009; Pascale et al. 2009). Middle: Radio spectral index,  $\alpha$ , in the six redshift bins. The mean value is  $-0.75 \pm 0.06$  and there is no evidence of significant evolution across  $0 < z < 3$ . Bottom:  $q_{250}$  and  $q_{\text{IR}}$  in the six redshift bins. Dashed line: weighted least-squares fit of the form  $q_{\text{IR}} \propto (1+z)^{-0.15}$ ; shaded area:  $\pm 1\sigma$  prediction of the Lacey et al. (2008) galaxy-formation model and the spectrophotometric model of Silva et al. (1998) for galaxies with  $L_{\text{IR}} > 10^{12} L_{\odot}$ , as implemented by Swinbank et al. (2008), updated to reflect our wavelength coverage and definition of  $q_{\text{IR}}$ .  $K$ -corrections are based on the measured radio spectra and – for  $q_{250}$  only – the SED discussed in Section 4.3 and shown in Fig. 9. The scale is chosen to match Fig. 12.

Swinbank et al. (2008) used the GALFORM semi-analytical galaxy-formation model to predict mild evolution of  $q_{\text{IR}}$  for luminous starbursts due to the  $\sim 5$ -Myr timelag between the onset of star formation and the resulting supernovae, in keeping with the mild evolution

claimed by Kovács et al. (2006) on the basis of 350- $\mu\text{m}$  observations of 15 SMGs. Kovács et al. suggested that a change of the radio spectral index might account for the deviation in  $q$ . Revisiting the GALFORM work of Swinbank et al. (2008) – calculating  $S_{\text{IR}}$  and  $q_{\text{IR}}$  for galaxies with  $L_{\text{IR}} > 10^{12} L_{\odot}$  in a manner consistent with this work – results in evolution of the form shown by the shaded area in Fig. 11 (lower panel), i.e. the evolution progresses in the opposite sense to that seen, with quantitative agreement only in the  $2 < z < 3$  regime.

The evolution seen here has implications for all the areas that rely on the FIR/radio correlation, e.g. the median redshift of SMGs determined via the oft-used  $S_{850\mu\text{m}}/S_{1400\text{MHz}}$  flux density ratio would be lower. It will be interesting to discover whether the evolution we report is confirmed by *Herschel* in the deepest multifrequency radio fields (e.g. Owen & Morrison 2008).

Taking the average properties of the 24- $\mu\text{m}$ - and 250- $\mu\text{m}$ -selected samples to be representative, so  $q_{\text{IR}} = 2.54 \pm 0.26$ , we can suggest a simple transformation between radio flux density and SFR, appropriate for samples in which radio-loud AGN constitute only a small fraction: a radio flux density of  $S_{1400\text{MHz}} (\text{W m}^{-2} \text{ Hz}^{-1})$  can be converted into a bolometric IR flux (rest-frame 8–1000  $\mu\text{m}$  in  $\text{W m}^{-2}$ ) via

$$S_{\text{IR}} = 10^{12.57 + (2.54 \pm 0.26)} S_{1400\text{MHz}}, \quad (5)$$

and thence into a SFR via

$$\text{SFR} = \Psi 10^{-10} \frac{4\pi d_{\text{lum}}^2 S_{\text{IR}}}{3.83 \times 10^{26}} \text{ M}_{\odot} \text{ yr}^{-1}, \quad (6)$$

where  $\Psi$  is 1.7 for a Salpeter IMF [ $dN(m)/dm = -2.35$ ] covering 0.1–100  $\text{M}_{\odot}$  (Condon 1992; Kennicutt 1998a,b; see also Scoville & Young 1983; Thronson & Telesco 1986; Inoue, Hirashita & Kamaya 2000).

#### 4.5 Stacking at the positions of sub-mJy radio galaxies

The value of  $q_{\text{IR}}$  found in the previous section is weighted by the types of galaxies found in the 24- $\mu\text{m}$  catalogue. To investigate whether  $q_{\text{IR}}$  is different for a radio-selected population, we stack the FIR/submm images at the positions of 816 robust radio emitters ( $> 5\sigma$ ,  $40 < S_{1400\text{MHz}} < 1000 \mu\text{Jy}$ ), divided into seven flux density bins, spaced evenly in  $\log_{10} S_{1400\text{MHz}}$ .

The FIR SEDs of the radio-selected galaxies are qualitatively similar to those of low-redshift 24- $\mu\text{m}$ -selected galaxies (compare the *top* panels of Figs 11 and 12). We find that  $q_{250}$  and  $q_{\text{IR}}$  are lower for radio-selected galaxies than for those selected in the mid-IR or FIR wavebands (Table 3), as one might expect given the selection criterion. However, the difference is surprisingly small: for  $40 < S_{1400\text{MHz}} < 100 \mu\text{Jy}$ , we obtain  $q_{250} = 2.42$  and  $q_{\text{IR}} = 2.25$ , cf. the equivalent (pre- $K$ -correction) values for our FIR-selected galaxy sample,  $q_{250} = 2.26 \pm 0.35$  and  $q_{\text{IR}} = 2.40 \pm 0.29$ . Bear in mind that, at a redshift of unity,  $q_{\text{IR}}$  would rise by  $\sim 0.06$  due to the radio  $K$ -correction and fall by  $\sim 0.15$  due to the shift of  $\lambda_{\text{rest}} = 8\text{--}1000 \mu\text{m}$  to lower observed frequencies – an overall shift of  $\sim -0.1$ . This suggests that star formation plays a significant role in powering faint radio galaxies, providing over half of their IR luminosity. Radio selection will inevitably have favoured galaxies with recently injected relativistic electrons so this is likely to be a lower limit. We find that  $q_{250}$  and  $q_{\text{IR}}$  anticorrelate with radio flux density (Fig. 12, lower panel), and we suggest this is due to the increasing prevalence of radio-loud AGN as one moves into the mJy regime (e.g. Ibar et al. 2009).

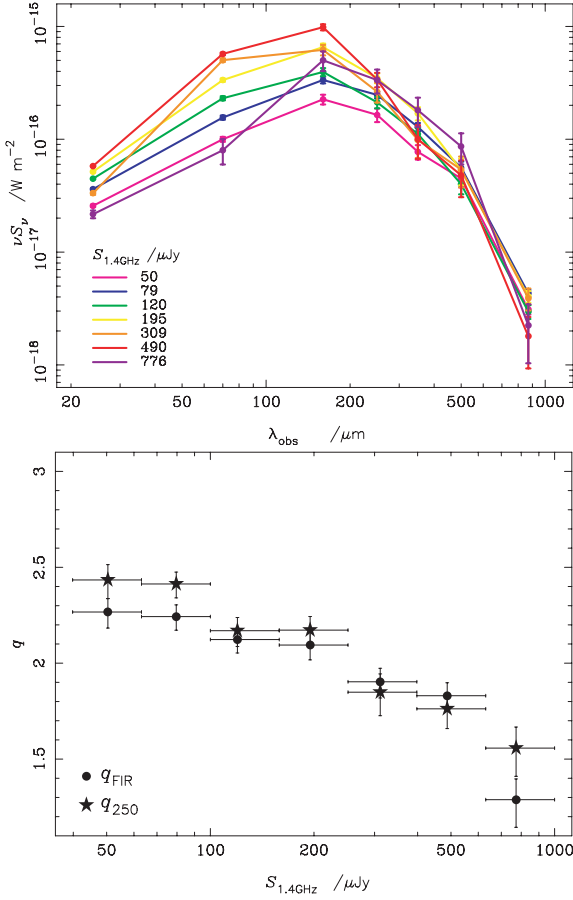


**Figure 12.** Top:  $\nu S_{\nu}$  versus observed wavelength, determined by stacking into the IR/submm images at the positions of faint radio emitters, in seven flux density bins, spaced evenly in  $\log_{10} S_{1400\text{ MHz}}$ . Median flux densities in each bin are reported in the key. Bottom:  $q_{250}$  and  $q_{\text{FIR}}$  in the seven flux density bins.  $K$ -corrections were not applied because complete redshift information was not available. The scale was chosen to match Fig. 11 (bottom).

## 5 CONCLUSIONS

We have defined a sample of 250- $\mu\text{m}$ -selected galaxies using data from BLAST. The noise is dominated by confusion, which severely limits the number of robust detections and hampers the identification of secure, unambiguous mid-IR or radio counterparts. These problems were not always apparent when using an objective, probabilistic approach to cross-identifying the galaxies.

We find that the most likely 24- $\mu\text{m}$  counterparts to our small sample of 250- $\mu\text{m}$  galaxies have a median [interquartile] redshift of 0.74 [0.25, 1.57].

At  $z \approx 0.6$ , where the BLAST 250- $\mu\text{m}$  filter probes rest-frame 160- $\mu\text{m}$  emission, we find no evidence for evolution of  $q_{250}$  relative to  $q_{160}$  measured for the SINGS sample of local galaxies.

We find that  $S_{\text{IR}}$  is better correlated with radio flux density than  $S_{250\mu\text{m}}$ , and that  $K$ -correcting the radio luminosity using measured spectral slopes reduces the scatter in the correlation.

$q_{\text{IR}}$  – the logarithmic ratio of bolometric IR and monochromatic radio fluxes – is determined for FIR-, mid-IR and radio-selected galaxies. We provide a simple recipe to convert a radio flux density into an instantaneous SFR, via bolometric IR luminosity, for mid-IR- or FIR-selected samples that do not contain a large fraction of radio-loud AGN.

$q_{\text{IR}}$  is found to be similar for our 250- $\mu\text{m}$ - and radio-selected galaxies, which suggests that star formation is responsible for over half of the IR luminosity in the latter, especially the faintest radio galaxies ( $S_{1400\text{ MHz}} < 100\ \mu\text{Jy}$ ). This fraction could well be higher given that radio selection favours galaxies with recent injections of relativistic electrons.

Stacking into 610- and 1400-MHz images at the positions of 24- $\mu\text{m}$ -selected galaxies, we find no evidence that the spectral slope at radio wavelengths evolves significantly across  $0 < z < 3$ . However, we find tentative evidence that  $q_{\text{IR}}$  does evolve, even across  $0 < z < 1$  where incompleteness in the parent sample should not be a serious issue. The evolution is of the form,  $q_{\text{IR}} \propto (1+z)^{-0.15 \pm 0.03}$ , across the peak epoch of galaxy formation. This has major implications for many techniques that rely on the FIR/radio correlation. We compare with semi-analytical model predictions and speculate that we may be seeing an increase in radio activity amongst ordinary, star-forming galaxies – relative to their IR emission – amongst that has been suggested may give rise to the radio background (Fixsen et al. 2009; Singal et al. 2009).

It will remain difficult to associate galaxies detected in *Herschel*/SPIRE surveys unambiguously with IR or radio counterparts, since the modest increase in telescope aperture and the steep source counts will ensure that confusion remains an issue (Devlin et al. 2009). However, alongside 70-, 100- and 160- $\mu\text{m}$  imaging from *Herschel*/PACS and 450- and 850- $\mu\text{m}$  SCUBA-2 data from the 15-m James Clerk Maxwell Telescope, it should be possible to fine-tune the astrometry to  $\sigma \sim 1$  arcsec and to deblend sources in deep SPIRE images. For the  $\sim 1\text{--}2\text{ deg}^2$  of FIR/submm coverage planned for the fields with the deepest available radio and *Spitzer* data, e.g. GOODS, the Subaru/*XMM-Newton* Deep Survey and the Lockman Hole, with  $\sigma_{1400\text{ MHz}} \lesssim 5\ \mu\text{Jy beam}^{-1}$  and  $\sigma_{24\mu\text{m}} \lesssim 10\ \mu\text{Jy}$  (Biggs & Ivison 2006; Miller et al. 2008; Owen & Morrison 2008; Morrison et al., in preparation; Arumugam et al., in preparation), almost every deblended FIR source should have relatively secure 24- $\mu\text{m}$  and radio identifications, the majority unambiguous, providing a complete redshift distribution and less biased estimates of  $q_{\text{IR}}$  for FIR-selected galaxies.

## ACKNOWLEDGMENTS

We thank John Peacock for his patient and good-natured assistance. We acknowledge the support of the UK Science and Technology Facilities Council (STFC), NASA through grant numbers NAG5-12785, NAG5-13301, and NNGO-6G11G, the NSF Office of Polar Programs, the Canadian Space Agency, and the Natural Sciences and Engineering Research Council (NSERC) of Canada.

## REFERENCES

- Appleton P. N. et al., 2004, *ApJS*, 154, 147
- Barger A. J., Cowie L. L., Sanders D. B., Fulton E., Taniguchi Y., Sato Y., Kawara K., Okuda H., 1998, *Nat*, 394, 248
- Bell E. F., 2003, *ApJ*, 586, 794
- Bernet M. L., Miniati F., Lilly S. J., Kronberg P. P., Dessauges-Zavadsky M., 2008, *Nat*, 454, 302
- Biggs A. D., Ivison R. J., 2006, *MNRAS*, 371, 963
- Blain A. W., Longair M. S., 1993, *MNRAS*, 264, 509
- Blain A. W., Ivison R. J., Smail I., 1998, *MNRAS*, 296, L29
- Carilli C. L., Yun M. S., 1999, *ApJ*, 513, L13
- Chapman S. C., Blain A. W., Smail I., Ivison R. J., 2005, *ApJ*, 622, 772
- Condon J. J., 1974, *ApJ*, 188, 279
- Condon J. J., 1992, *ARA&A*, 30, 575
- Coppin K. E. K. et al., 2009, *MNRAS*, 395, 1905

- Croom S. M., Warren S. J., Glazebrook K., 2001, *MNRAS*, 328, 150
- Dale D. A. et al., 2007, *ApJ*, 655, 863
- de Jong T., Klein U., Wielebinski R., Wunderlich E., 1985, *A&A*, 147, L6
- Desai V. et al., 2007, *ApJ*, 669, 810
- Devlin M. J. et al., 2009, *Nat*, 458, 737
- Dickey J. M., Salpeter E. E., 1984, *ApJ*, 284, 461
- Dickinson M., Giavalisco M., The GOODS Team, 2003, in Bender R., Renzini A., eds, *The Mass of Galaxies at Low and High Redshift*. Springer, Berlin, p. 324
- Donley J. L., Rieke G. H., Rigby J. R., Pérez-González P. G., 2005, *ApJ*, 634, 169
- Downes A. J. B., Peacock J. A., Savage A., Carrie D. R., 1986, *MNRAS*, 218, 31
- Dunlop J. S., Peacock J. A., 1990, *MNRAS*, 247, 19
- Dunne L., Eales S., Edmunds M., Ivison R., Alexander P., Clements D. L., 2000, *MNRAS*, 315, 115
- Dunne L. et al., 2009a, *MNRAS*, 394, 3
- Dunne L. et al., 2009b, *MNRAS*, 394, 1307
- Dye S. et al., 2009, preprint (arXiv:0904.1204)
- Eales S. et al., 2009, preprint (arXiv:0907.4156)
- Fixsen D. J., Dwek E., Mather J. C., Bennett C. L., Shafer R. A., 1998, *ApJ*, 508, 123
- Fixsen D. J. et al., 2009, preprint (arXiv:0901.0555)
- Frayser D. T. et al., 2006, *ApJ*, 647, L9
- Frayser D. T. et al., 2009, preprint (arXiv:0902.3273)
- Greve T. R. et al., 2009, *ApJ*, submitted (arXiv:0904.0028)
- Griffin M. et al., 2009, in Pagani L., Gerin M., eds, *EAS Publications Series*, Vol. 34, *Astronomy in the Submillimeter and Far Infrared Domains with the Herschel Space Observatory*. EDP Sciences, Les Ulis, p. 33
- Helou G., Soifer B. T., Rowan-Robinson M., 1985, *ApJ*, 298, L7
- Hughes D. H. et al., 1998, *Nat*, 394, 241
- Ibar E. et al., 2008, *MNRAS*, 386, 953
- Ibar E., Ivison R. J., Biggs A. D., Lal D. V., Best P. N., Green D. A., 2009, *MNRAS*, 397, 281
- Inoue A. K., Hirashita H., Kamaya H., 2000, *PASJ*, 52, 539
- Ivison R. J. et al., 2002, *MNRAS*, 337, 1
- Ivison R. J. et al., 2007a, *ApJ*, 660, L77
- Ivison R. J. et al., 2007b, *MNRAS*, 380, 199
- Kennicutt R. C. Jr, 1998a, *ARA&A*, 36, 189
- Kennicutt R. C. Jr, 1998b, *ApJ*, 498, 541
- Kovács A., Chapman S. C., Dowell C. D., Blain A. W., Ivison R. J., Smail I., Phillips T. G., 2006, *ApJ*, 650, 592
- Lacey C. G., Baugh C. M., Frenk C. S., Silva L., Granato G. L., Bressan A., 2008, *MNRAS*, 385, 1155
- Le Fèvre O. et al., 2004, *A&A*, 428, 1043
- Lehmer B. D. et al., 2005, *ApJS*, 161, 21
- Luo B. et al., 2008, *ApJS*, 179, 19
- Magnelli B., Elbaz D., Chary R. R., Dickinson M., Le Borgne D., Frayer D. T., Willmer C. N. A., 2009, *A&A*, 496, 57
- Marsden G. et al., 2009, preprint (arXiv:0904.1205)
- Miller N. A., Fomalont E. B., Kellermann K. I., Mainieri V., Norman C., Padovani P., Rosati P., Tozzi P., 2008, *ApJS*, 179, 114
- Owen F. N., Morrison G. E., 2008, *AJ*, 136, 1889
- Pascale E. et al., 2009, preprint (arXiv:0904.1206)
- Patanchon G. et al., 2009, preprint (arXiv:0906.0981)
- Poglitsch A. et al., 2008, *Proc. SPIE*, 7010, 701005
- Pope A. et al., 2006, *MNRAS*, 370, 1185
- Puget J.-L., Abergel A., Bernard J.-P., Boulanger F., Burton W. B., Desert F.-X., Hartmann D., 1996, *A&A*, 308, L5
- Rengarajan T. N., 2005, preprint (astro-ph/0511156)
- Scoville N., Young J. S., 1983, *ApJ*, 265, 148
- Seiffert M. et al., 2009, preprint (arXiv:0901.0559)
- Silva L., Granato G. L., Bressan A., Danese L., 1998, *ApJ*, 509, 103
- Singal J., Stawarz L., Lawrence A., Petrosian V., 2009, preprint (arXiv:0909.1997)
- Smail I., Ivison R. J., Blain A. W., 1997, *ApJ*, 490, L5
- Smail I., Ivison R. J., Owen F. N., Blain A. W., Kneib J.-P., 2000, *ApJ*, 528, 612
- Spergel D. N. et al., 2007, *ApJS*, 170, 377
- Swinbank A. M. et al., 2008, *MNRAS*, 391, 420
- Symeonidis M., Page M. J., Seymour N., Dwelly T., Coppin K., McHardy I., Rieke G. H., Huynh M., 2009, *MNRAS*, 397, 1728
- Szokoly G. P. et al., 2004, *ApJS*, 155, 271
- Thronson H. A. Jr, Telesco C. M., 1986, *ApJ*, 311, 98
- Truch M. D. P. et al., 2009, preprint (arXiv:0904.1202)
- van der Kruit P. C., 1971, *A&A*, 15, 110
- Vanzella E. et al., 2008, *A&A*, 478, 83
- Weiss A. et al., 2009, *ApJ*, submitted

This paper has been typeset from a  $\text{\LaTeX}$  file prepared by the author.